Review

Nanostructure Engineering of Alloy-Based Anode Materials with Different Dimensions for Sodium/Potassium Storage

Xiaolong Cheng [1], Dongjun Li [2], Yu Jiang [1,*], Fangzhi Huang [1,*] and Shikuo Li [1,*]

1   School of Material Science and Engineering, Anhui University, Hefei 230601, China; chengxl@ahu.edu.cn
2   Department of Materials Science and Engineering, CAS Key Laboratory of Materials for Energy Conversion, University of Science and Technology of China, Hefei 230026, China; ldj0226@mail.ustc.edu.cn
*   Correspondence: jiangyu21@ahu.edu.cn (Y.J.); hfz@ahu.edu.cn (F.H.); lishikuo@ahu.edu.cn (S.L.)

Abstract: Sodium/potassium-ion batteries have drawn intensive investigation interest from researchers owing to their abundant element resources and significant cost advantages. Anode materials based on alloy reaction mechanisms have the prominent merits of a suitable reaction potential and high theoretical specific capacity and energy density. However, very large volumetric stresses and volume changes during the charge/discharge process and the resulting electrode structural cracking, deactivation and capacity fading seriously hinder their development. To date, a series of modification strategies have been proposed to tackle these challenges and achieve good electrochemical performance. Herein, we review the recent advances in the structural engineering of alloy-type anodes for sodium/potassium storage, mainly including phosphorus, tin, antimony, bismuth and related alloy materials, from the perspective of dimensional structure. Furthermore, some future research directions and unresolved issues are presented for the investigation of alloy-based anode materials. It is hoped that this review can serve as a guide for the future development and practical application of sodium/potassium-ion batteries.

Keywords: alloy-type anodes; sodium-ion batteries; potassium-ion batteries; structural engineering; dimensional structure

1. Introduction

In recent decades, lithium-ion batteries have developed rapidly and changed people's lifestyles [1–5]. However, with the rapid rise in energy storage demand, problems such as scarce lithium resource reserves in the Earth's crust (0.0065 wt%), uneven global distribution (≈40% in South America) and soaring lithium salt prices have become increasingly prominent, prompting researchers to explore the next generation of efficient and low-cost energy storage systems [6–8]. As elements in the same main group as lithium (Li), sodium (Na) and potassium (K) have analogous chemical properties and similar redox potentials to lithium [9–12]. Typically, the standard redox potentials of Li^+/Li, Na^+/Na and K^+/K versus a standard hydrogen electrode (SHE) are close to each other: –3.04 V, –2.71 V and –2.93 V, respectively [13–15]. In terms of element reserves, the reserves of Na (2.36 wt%) and K (2.09 wt%) are much more abundant than those of Li, and they are widely distributed around the world [16,17]. In addition, the operating mechanism of sodium-ion batteries (SIBs) and potassium-ion batteries (PIBs) is the same as that of lithium-ion batteries (LIBs), known as the "rock-chair" operating mechanism. Therefore, SIBs and PIBs are considered as two of the most promising alternatives to LIBs [17–19].

From the perspective of battery structure and composition, SIBs and PIBs are similar to LIBs, including the cathode, anode, current collector, separator, electrolyte and other parts. Due to the inability of sodium and potassium to alloy with aluminum (Al), cheaper metallic Al foil can be employed as the anodic current collector of SIBs and PIBs, which further reduces the cost of energy storage systems. For both the separator and electrolyte systems of SIBs and PIBs, LIBs can be referred to because of their similar operating mechanisms. It is worth noting that Na^+ and K^+ have larger ionic radii than Li^+ (102, 138 and 76 pm, respectively), which results in slower reaction kinetics and greater structural damage to the electrode material [20–22].

Therefore, suitable electrodes are extremely important in the development of SIBs and PIBs. After years of research, impressive achievements have been made in cathode materials for SIBs and PIBs, including layered metal oxides [23–26], polyanionic compounds [27–29], Prussian blue analogs [30–32] and organic compounds [33–35]. However, there are still many problems in terms of anode materials, which have become a key factor limiting the progress of SIBs and PIBs. Based on a review of recent research, negative electrode materials can be classified into the following categories based on their reaction mechanisms: the intercalation type, the conversion type and the alloy type [36–38]. Alloy-type anode materials, such as phosphorus (P), tin (Sn), antimony (Sb) and bismuth (Bi), have drawn much attention owing to their high specific capacity, low operating voltage and high energy density. Unfortunately, despite these advantages, alloy-based anode materials still suffer from some intrinsic disadvantages that affect their practical applications. On the one hand, the high Na/K storage capacity of alloy-based anode materials is still accompanied by very large volumetric stresses and volume changes during repeated cycling [39–41]. During the cycling process, the expansion and contraction of electrode materials can cause the pulverization and loss of electrical contact of the active materials, as well as the fragmentation and deactivation of the electrodes, which will seriously affect the lifespan of the full cell. On the other hand, the diffusion kinetics of Na^+/K^+ in alloy-type materials during the reaction process is sluggish, which will limit the rate performance of the electrode. For some specific elements, such as P, their low electrical conductivity is also a key factor limiting their development. To address these issues, researchers made considerable efforts such as controlling the particle size, incorporating carbon materials, constructing favorable nanostructures and developing compatible electrolytes. A review of relevant research articles in recent years shows that a large number of structural engineering studies have been carried out to adjust the physicochemical properties of the electrode surface and interface and improve the electrochemical performance.

In this progress report, we review the key advances of alloy-based anode materials for SIBs and PIBs with a primary emphasis on nanosizing, low-dimensional structure and other special nanostructure designs. According to the dimensionality, we classify the nanostructures as zero-dimensional (0D), one-dimensional (1D), two-dimensional (2D) or three-dimensional (3D), as shown in Figure 1. We summarize various nanostructures as well as the structure–property relationships of alloy-based anode materials. Finally, we also share our views on some unsolved problems and development directions in the investigation of alloy-based anodes for the industrial application of high-performance SIBs and PIBs.
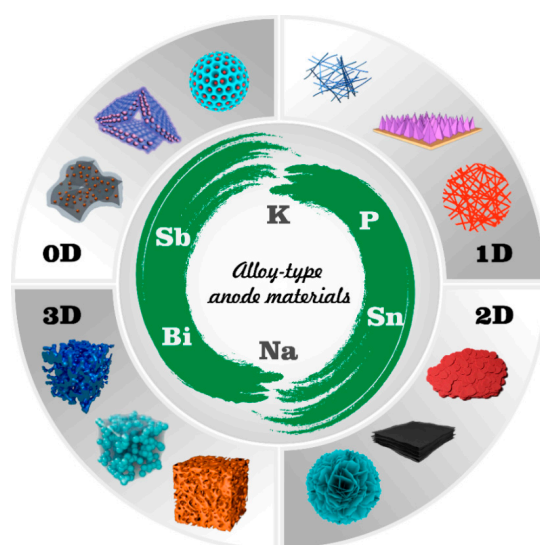

Figure 1. The schematic diagram of alloy-type anode materials classified into 0D, 1D, 2D, 3D for SIBs and PIBs. Reproduced with permission from Refs. [42–44], copyright 2018, 2020, 2021, American Chemical Society; from Refs. [45–50], Copyright 2019, 2021, 2023, Wiley-VCH; from Ref. [51], Copyright 2021, Elsevier; from Refs. [52,53], Copyright 2023, The Royal Society of Chemistry.

2. Characteristics and Challenges

The choice of alloy-based anode materials for SIBs and PIBs is primarily in the IV A and V A group, including P, Sn, Sb, Bi, etc. Figure 2 shows the crystal structure of various alloy-based anode materials. Thereinto, P has many allotropes, which mainly include white P (WP), red P (RP) and black P (BP). WP cannot be used as anode materials, due to its highly toxic, unstable chemical properties. BP has the best thermodynamic stability under ambient conditions. BP has a two-dimensional layered structure (Figure 2a) and high electrical conductivity (300 S cm^{-1}). Commercial red P is nontoxic and low-cost, which is promising for application as anode materials for SIBs and PIBs. However, its low electrical conductivity (10^{-14} S cm^{-1}) restricts it development. In addition to commercial red phosphorus, there are other allotropes of red phosphorus, such as crystalline fiber phosphorus (FP) (Figure 2b) and violet phosphorus (VP) (Figure 2c). Except for P-based anodes, Sn, Sb and Bi are all metallic elements and have good electrical conductivity. Sn-based anodes have also been widely investigated in SIBs and PIBs owing to their high specific capacity, high abundance and nontoxicity (Figure 2d). As shown in Figure 2e,f, both Sb and Bi have layered crystal structures. When used as anode materials for SIBs and PIBs, Sb and Bi show advantages of high specific capacities and low operation potential.
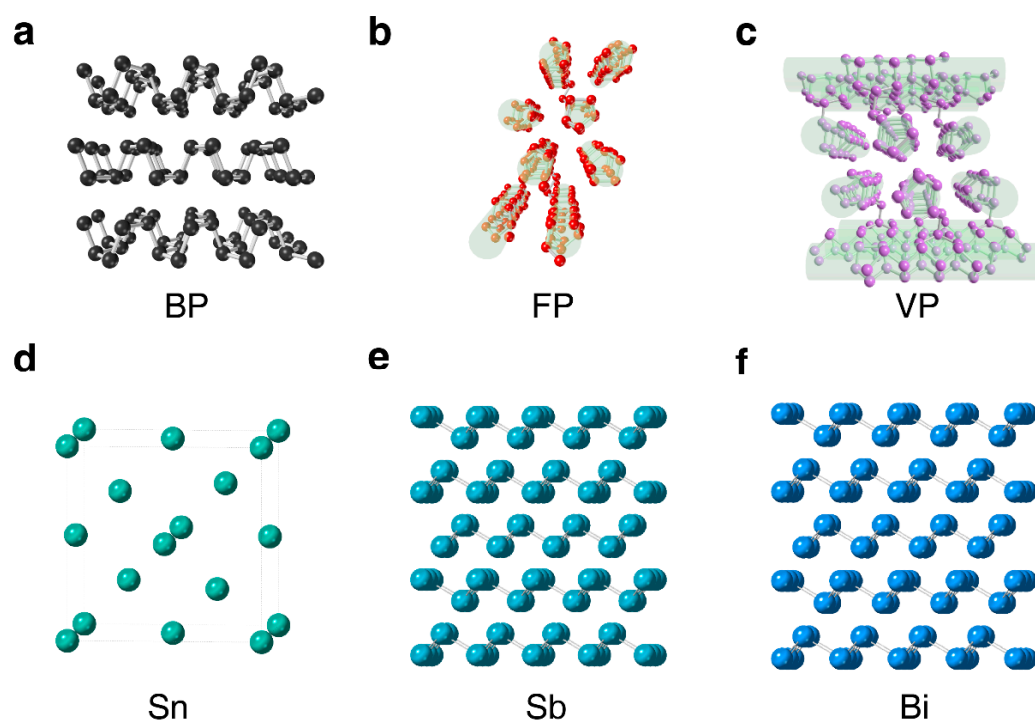

Figure 2. Crystal structure of BP (**a**), FP (**b**), VP (**c**), Sn (**d**), Sb (**e**) and Bi (**f**).

In general, alloy-type materials, including P, Sn, Sb and Bi, can react with Na/K via alloy reaction, delivering high theoretical capacity. However, with the sodiation/potassiation process, the alloy-type anode will undergo a very large volume expansion due to the alloy-reaction-induced phase transformation. Table 1 summarizes the specific capacity and volume expansion rate of different alloy-type materials during the sodiation and potassiation process. For material particles, a very large volume expansion will cause pulverization of the particles. Exposed fresh interfaces will continuously consume the electrolyte and produce solid electrolyte interface (SEI) film. After some particles are wrapped by SEI film, they will lose electrical contact and thus lose activity. For electrodes, the volume expansion of the materials will cause stress inside the electrode. In some severe cases, the electrode will crack or even detach from the current collector. Therefore, achieving a stable structure and fast reaction kinetics through reasonable structural design is very important for the development of alloy-based anodes.

Table 1. The characteristics of various alloy-type anode materials for SIBs and PIBs.

Elements	Application	Sodiation/Potassiation Products	Specific Capacity (mAh g^{-1})	Volume Expansion Ratio (%)
P	SIBs	Na$_3$P	2596	490
	PIBs	KP	865	232
		K$_4$P$_3$	1154	293
		K$_3$P	2596	593
Sn	SIBs	Na$_{15}$Sn$_4$	847	423
	PIBs	KSn	225	194
Sb	SIBs	Na$_3$Sb	660	393
	PIBs	K$_3$Sb	660	407
Bi	SIBs	Na$_3$Bi	385	352
	PIBs	K$_3$Bi	385	509

3. Nanostructural Design

In recent decades, nanomaterials have developed rapidly in alkali metal ion batteries, benefited by significant size effects and surface effects compared to macroscopic bulk materials. In order to achieve the structural stability of materials under actual working conditions, a variety of creative nanostructure designs continue to emerge. Nanostructured materials are a kind of low-dimensional material with nanoscale size at least in one direction [54]. According to their structural characteristics, nanomaterials can be roughly constituted into 0D, 1D, 2D and 3D materials. In the structural design of alloy-type anode materials, nanomaterials with different dimensional structures have respective unique advantages and play a significant role in improving electrochemical performance. Thus, we review the various nanostructure designs and the investigate the mechanisms of nanostructure alloy-type anode materials for SIBs and PIBs.

In the development process of alloy-based anodes, various synthesis methods are employed to achieve electrode materials with unique nanostructures, including hydrothermal/solvothermal methods, annealing, ball-milling, wet-chemistry routes, etc. Thereinto, P has many different physiochemistry properties in comparison with other metallic alloy-type anode materials, which leads to different synthesis processes. The vaporization–condensation method is a typical synthesis process for P-C composites, which effectively encapsulates P into the porous structure of carbon hosts, significantly improving the electronic conductivity of the composites [55]. For the synthesis of metallic alloy-type anodes, such as Sn, Sb, Bi and some binary alloys, many synthesis methods have been developed. Thereinto, annealing techniques are usually used for carbon-coated metallic nanoparticles. A solution-based replacement reaction and dealloying method are usually used for unique dimensional structures including 1D, 2D and 3D [47]. In addition, owing to the layered crystal structure of BP, Sb and Bi, exfoliation techniques are often used to generate ultrathin 2D nanomaterials [56,57].

3.1. 0D Materials: Nanodots, Nanoparticles, Nanospheres

According to the dimensionality of nanostructure materials, the 0D materials are defined as materials with nanoscale dimensions in all three directions, including nanodots, nanoparticles, nanospheres, etc. Because of its extremely small size in all directions and very large specific surface area, 0D materials exhibit significant advantages in the field of electrochemistry. The small size of the 0D materials can facilitate mass transfer via a shortened transmission path in the electrochemical reaction. The very large specific surface area can provide abundant ionic adsorption sites. When used as anode materials with alloy reaction mechanisms, the 0D materials have additional advantages for buffering very large volume expansions. In the research process of alloy-based anodes for LIBs, it is found that the fracture of silicon during lithiation is closely related to the size of Si particles [58]. When the diameter of Si particles is below ~150 nm, particle cracking and fracture do not occur, which is due to the stored strain energy being insufficient to drive crack propagation

during the lithiation process. Compared with LIBs, the alloy-type anode materials suffer a much more severe volumetric stress and greater volume expansion. Therefore, a lot of research has been devoted to downsizing the particle of the alloy-type anode materials, developing a variety of 0D materials, including nanospheres, nanoparticles, nanodots, etc.

Due to low intrinsic conductivity of red P, researchers usually construct the structure of carbon-modified RP nanoparticles. Graphene and carbon nanotubes (CNTs) are two kinds of typical carbon nanomaterials with very large specific surface areas and high electric conductivities. After dispersing RP nanoparticles (5–10 nm) on the surface of reduced graphene oxide (rGO) via the phosphorus-amine-based method with durable loading ratio and high yield, the RP-based anode offers a high specific capacity of 2057 mAh g^{-1} at a current density of 0.1 A g^{-1} and long lifespan for 5000 cycles [59].

By anchoring the RP@BP nanoparticles on 3D N-doped graphene, the composites (RP@BP/3DNG) exhibit high electronic conductivity. In addition, the heterointerfaces of the RP@BP nanoparticles generate a built-in electric field and thus lower the Na^+ diffusion barrier. When evaluated as anodes of SIBs, the RP@BP/3DNG delivers outstanding electrochemical performance, including rate performance (with a capacity retention of 521.3 mAh g^{-1} at current density of 10 A g^{-1}) and a long lifespan (with a specific capacity of 465.5 mAh g^{-1} remaining after 1200 cycles at current density of 10 A g^{-1}). Zhu et al. developed a hierarchical WDC/CNTs@RP electrode, achieving unprecedented rate performance [60]. The hierarchical nanostructure is based on a wood-derived carbon (WDC) framework with both low tortuosity and a highly crosslinked conductive 3D carbon nanotube (CNT) network, and the RP nanoparticles are incorporated with the WDC and CNTs (Figure 3a,b). This unique structure gives superior conductivity for both electrons and ions. When used as anode materials of the SIBs, the WDC/CNTs@RP shows a high capacity retention of 1.63 mAh cm^{-2} even at a high areal current density of 106.6 mA cm^{-2} (Figure 3c). The low tortuosity of the structure causes the mass loading of RP to reach up to 14.1 mg cm^{-2}. Figure 3d shows the working mechanism of the electrode. The WDC and CNTs provide a fast electron transport path and the vertical channels filled with electrolyte can shorten the pathways of Na^+. Considering the ultrahigh electrical conductivity (about 10^{14} times that of the RP), Ma et al. reported a new red@black phosphorus core–shell heterostructure (RP@BP) via a one-step solvothermal strategy [61]. In a sense, the coupling of red phosphorus with graphene and CNTs is prone to failure during cycling, leading to the deactivation of active materials and fading of capacity. Therefore, researchers developed micro–mesoporous carbon materials to encapsulate the RP.

In order to buffer the high volume expansion during potassiation to within 293% (K_4P_3) or 593% (K_3P) compared to the RP phase, Xu et al. encapsulated RP into a carbon-nanotube-backboned mesoporous carbon and the composites with good cycling stability [62]. After downsizing the RP nanoparticles to 10–20 nm and encapsulating on a 3D porous carbon framework, the composite delivers an improved reversible capacity and superior rate capability [55]. Compared with SIBs, potassium storage causes a greater volume expansion and has stricter structural design requirements. The electrochemical performance, including rate capability and long cycle performance, is unsatisfactory, which is mainly due to sluggish K^+ diffusion kinetics and severe structure destruction. Therefore, in order to achieve better electrochemical performance, RP needs to be further nanosized. In 2021, the Sun group fabricated the RP nanoparticles embedded in a commercial porous carbon via the evaporation–condensation strategy (Figure 3e) [51]. The porous carbon with rich mesopores (mainly in range of 2.0–10 nm) and micropores not only facilitate electrolyte permeation but address the very large volume expansion of RP via inner void spaces. In addition, the nanosized RP embedded in the mesopores and micropores can further shorten the K^+ diffusion path and accelerate the reaction kinetics. Benefitting from the appropriate structural design, the P/C composites yield an improved electrochemical performance. When cycling at a current density of 0.1 A g^{-1}, the initial charging capacity can achieve 744 mAh g^{-1}. The lifespan under 3.2 A g^{-1} can maintain a capacity retention of 287 mAh g^{-1} after 10,000 cycles at 11.2 A g^{-1} (Figure 3f).

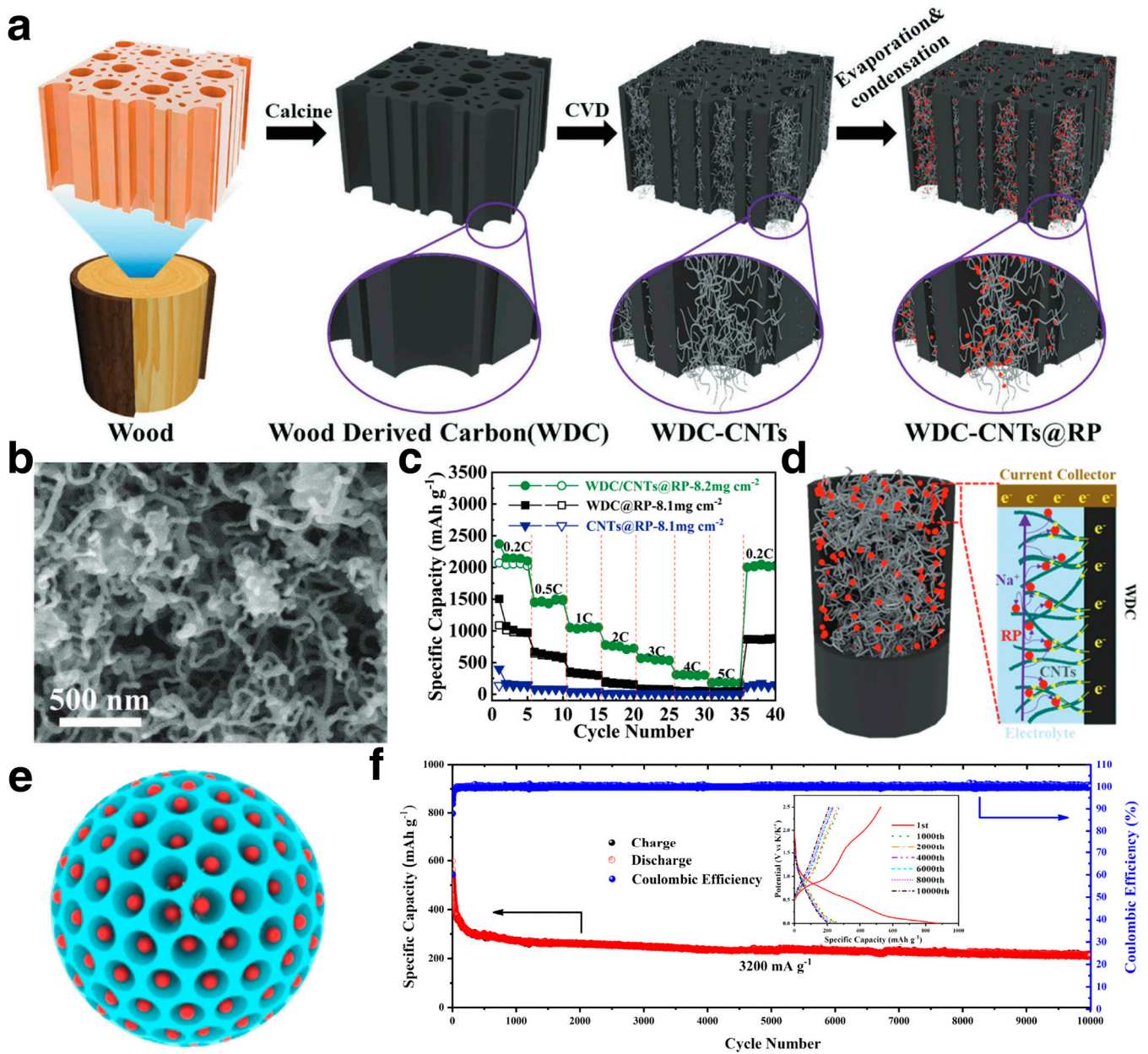**Figure 3.** (**a**,**b**) Schematic illustration of the synthesis and the SEM of the WDC/CNTs@RP electrode, respectively; (**c**) the rate performance comparison; (**d**) the schematic illustration of the electron/ion transfer mechanism of the WDC/CNTs@RP. Reproduced with permission [60]. Copyright 2022, Wiley-VCH. (**e**,**f**) The schematic illustration and the cycling performance of the P/C composite, respectively. Reproduced with permission [42]. Copyright 2022, Elsevier.

　　　The design methodology of the 0D structure is also applicable to the Sn-, Sb- and Bi-based anode materials to relieve the very large volume change during the charge and discharge process. As metallic elements, bulk Sn, Sb and Bi have benign electrical conductivity. However, the form of contact between the nanoparticles of Sn, Sb and Bi is point contact, which cannot stably transfer electrons during electrochemical reactions. Especially, an SEI film is generated on the nanoparticles, which is electronically insulated and causes the nanoparticles to lose electrical contact. Therefore, the 0D structure of the Sn, Sb and Bi usually cooperate with various kinds of conductive skeletons, such as graphene [63–66], CNT [67,68], porous carbon [65,69] and MXene [70,71], or is directly coated with a carbon layer [45,72]. Based on these considerations, Chen et al. use the "pinning effect" of NaCl to generate nanosized Sb particles in the carbon matrix. The well-designed nanos-

tructure offers enhanced electron/ion transport kinetics during electrochemical reactions (Figure 4a) [73]. When used for sodium storage, the Sb-based anode delivers a lifespan of over 20,000 cycles at 10 A g^{-1} with a capacity retention ratio of 98.9% (Figure 4b). It is interesting to note that the carbon matrix undergoes graphitization by the ion shuttle effect during the activation process (Figure 4c). Similarly, a composite of porous carbon matrix and Bi-Sb alloy nanoparticles (BiSb@C) was prepared via freeze-drying and the pyrolysis method with KCl as the template, which exhibited long cyclability at 0.2 and 0.5 A g^{-1} for 600 cycles when used as an anode for KIBs [65]. In addition to organic electrolyte systems, the Bi-based anode can be used for aqueous SIBs owing to its nonselective ion insertion and high theoretical capacity. Recently, Zhu and coworkers anchored Bi nanoparticles on graphene through chemical bonding via the laser-induced compounding method (Bi@LIG), as shown in Figure 4d. The Bi@LIG with a Bi-G heterostructure can not only release the volumetric stress, but also expose active materials and accelerate the reaction kinetics. In order to cope with the very large volume expansion, a cavity design is also applied in many works. A metal–organic framework (MOF)-derived yolk–shell Sb@C nanobox encapsulated in carbon nanofibers was synthesized via the electrospinning method (Figure 4e) [74]. The structure evolution process during potassiation/depotassiation was observed via in situ TEM, revealing that the void space effectively accommodates the expansion of Sb (Figure 4f). In addition, Yang et al. developed an efficient and cheap synthesis method for yolk–shell Sb/C composites via the reduction of polypyrrole-coated Sb$_2$O$_3$ [67]. The as-prepared Sb-based anode shows outstanding rate performance and stability in deep cycling.
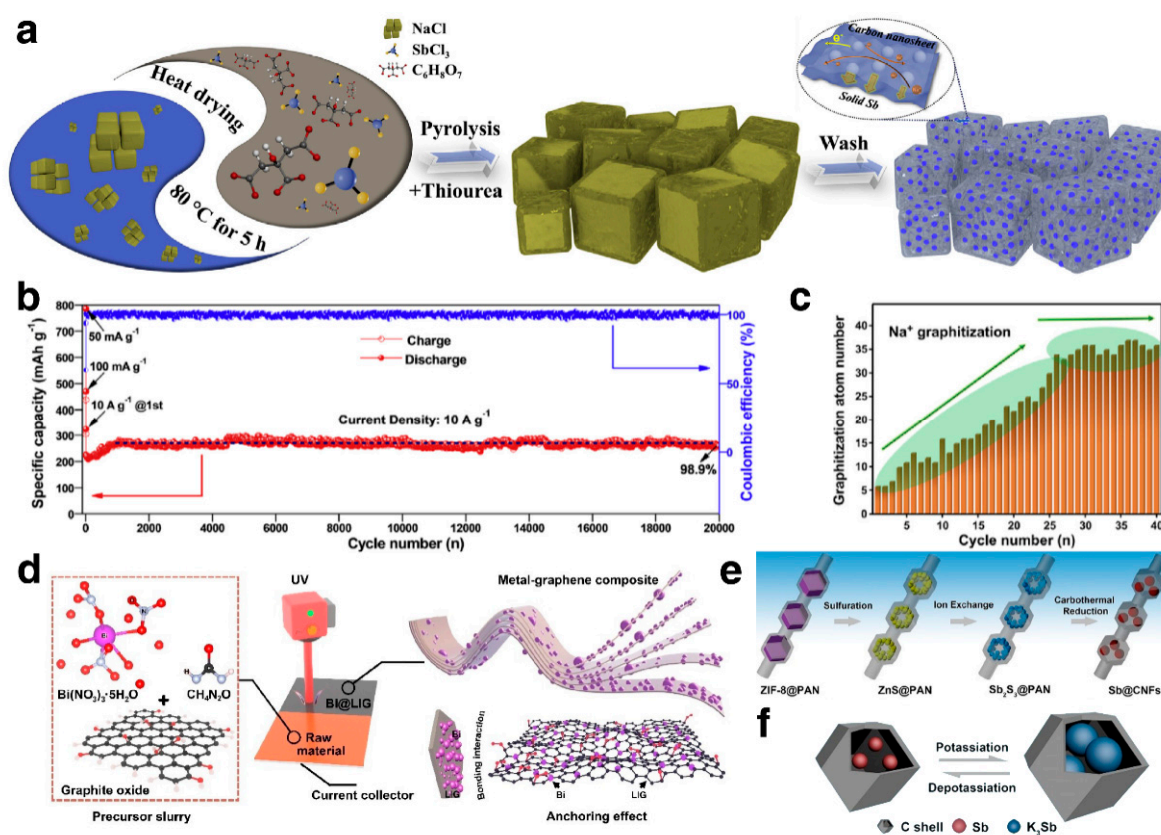

Figure 4. (**a**,**b**) The synthesis schematic illustration and cycling performance of the Sb@NS-3DPC; (**c**) ion-shuttle-induced graphitization. Reproduced with permission [73]. Copyright 2022, Elsevier. (**d**) The synthesis schematic illustration of the Bi@LIG. Reproduced with permission [63]. Copyright 2023, Wiley-VCH. (**e**) The synthesis schematic illustration of the Sb@CNFs; (**f**) schematic illustration of the reaction processes of the Sb@CNFs. Reproduced with permission [74]. Copyright 2020, Wiley-VCH.

3.2. 1D Materials: Nanowires, Nanorods, Nanofibers

One-dimensional materials are defined as the materials whose size in one of the three dimensions is above 100 nm. Reviewing articles published in recent years, we classify nanowires, nanorods, nanotubes, nanofibers and some nanoarrays as one-dimensional materials. One-dimensional materials have high specific surface area and short size in the radial direction. In terms of alloy-type anode materials, 1D materials can provide short ion diffusion paths and tolerate stress changes in the radial direction and fast electron transfer routines along the axial direction, which significantly accelerate the reaction kinetics. In addition, 1D materials like nanowires, nanotubes and nanofibers can improve the integrity and stability of the electrode. In recent years, extensive works have been carried out to develop 1D nanomaterials for alloy-type anodes of SIBs and PIBs. On the basis of these 1D nanostructures, the reaction mechanism of alloy-type materials and the dependency between the structure and performances are investigated comprehensively.

Carbon nanofibers (CNFs) and CNTs are two kinds of typical 1D nanomaterials with nanoscale radial dimensions and micron-scale axial dimensions. Compared with carbon nanoparticles, CNFs and CNTs can realize rapid electron conduction through mutual cross-linking and stable electrodes by virtue of their high aspect ratios and mechanical strength. As early as 2013, Dou's group already mixed microsized RP and CNTs, which shows a specific capacity of 1675 mAh g^{-1} for SIBs [75]. In this case, CNTs mainly play the role of conductive agent to deal with the problem of poor electrical conductivity of RP. Relevant studies have found that CNTs have a significant effect on improving the electrochemical properties of RP-based anode materials [76–78]. In 2019, Li et al. successfully encapsulated the phosphorus rings and chains into the multi-walled CNTs based on the facile conversion of RP into soluble polyphosphide anions in organic solvents by activating reactions with nucleophilic reagents [79]. The composite was applied to the anode of the LIBs and delivered outstanding electrochemical performance. Based on similar structural design ideas, RP was encapsulated into CNFs via the vaporization–condensation method [80]. In terms of nanostructure design, CNFs serve as a conductive shell and offer a fast electron transferring routine. Meanwhile, the reserved void can accommodate the volume expansion of the RP during the sodiation process. Compared with RP nanoparticles that have no regular shape, the 1D structure makes it easier to observe the sodiation behavior of RP. The sodiation process of the RP encapsulated in CNFs was observed via in situ TEM, which demonstrates a "liquid-like" mechanical property (Figure 5a). During sodiation, RP segments in the CNFs deformed and merged, confirming the sodiation-induced softening effect of RP. Figure 5b,c show the modeling results of the stress distribution of the CNF-constrained RP and a freestanding particle, which reveals that the CNFs exert the mechanical constraint effect on the stress mitigation of RP. As a comparison, the freestanding RP particles suffer higher stresses on the surface, which is mainly due to the pushing-out effect of RP particles during sodiation and the lack of mechanical constraint. When used as anode materials of SIBs, the 1D RP-based composites deliver outstanding long cycle performance (~1850 mAh g^{-1} at 0.1 A g^{-1} and over 1000 mAh g^{-1} at 1 A g^{-1} after over 5000 cycles). As an allotrope of red phosphorus, the FP with a regular crystal structure has a significantly increased electronic conductivity (approximately 10^8 times), which shows great prospects for improving the Na/K storage performance of the P-based anode materials. Recently, Zhu et al. found that trace amounts of selenium (Se) could induce the conversion of commercial RP into crystalline FP and developed a 1D FP nanostructure via a typical annealing procedure (Figure 5d) [50]. As shown in Figure 5e, the as-prepared FP exhibits a typical morphology of nanofibers with a diameter of ~100 nm and length of 2–3 μm. In addition, the Se-dopant can also improve the Na$^+$ ionic conductivity and enhance the structural stability via regulating the chemical state of P. When used as an anode for SIBs, the optimal FP delivers an outstanding rate capability with a specific capacity of 1190 mAh g^{-1} at 25 C and competitive cyclability with a capacity retention ratio of 90.1% at 1 C after 2800 cycles (Figure 5f,g).
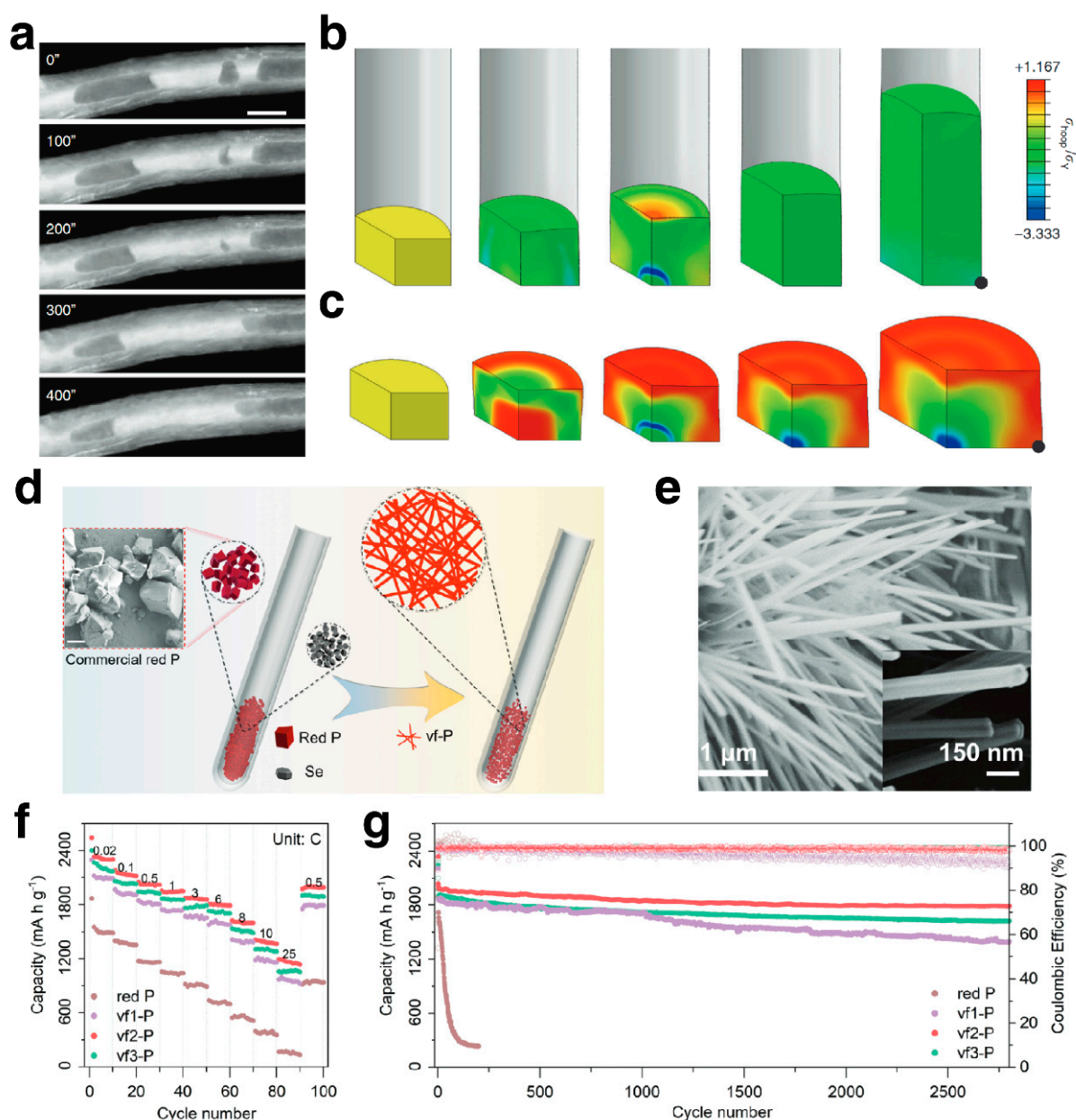
Figure 5. (**a**) STEM image series of the P_{red}@CNF during sodiation (scale bar is 100 nm); (**b,c**) stress distribution of the P_{red}@CNF and RP particle according to finite element modeling. Reproduced with permission [80]. Copyright 2020, Nature Publishing Group. (**d**) Schematic illustration of synthesis (scale bar is 20 μm), (**e–g**) SEM image and rate performance of the vf-P. Reproduced with permission [50]. Copyright 2023, Wiley-VCH.

In terms of metallic anode materials, such as Sn, Sb, Bi and corresponding binary alloy phases, 1D structures with a long axial dimension and short radial dimension can exert their conductivity and shorten the ion diffusion path. In recent years, a lot of investigations have been devoted to downsizing the dimension of alloy-type anode materials, and developing various 1D nanomaterials, such as carbon-coated nanowires, nanotubes, nanorods and nanoarrays. As shown in Figure 6a, Bi nanorods encapsulated in carbon nanotubes were fabricated via the reduction of Bi_2S_3 nanorods and the durable annealing condition [81]. When used for potassium storage, the carbon shell provides a fast electronic transfer pathway and the void can shorten the ionic diffusion distance and accommodate the volume expansion of the Bi nanorods.
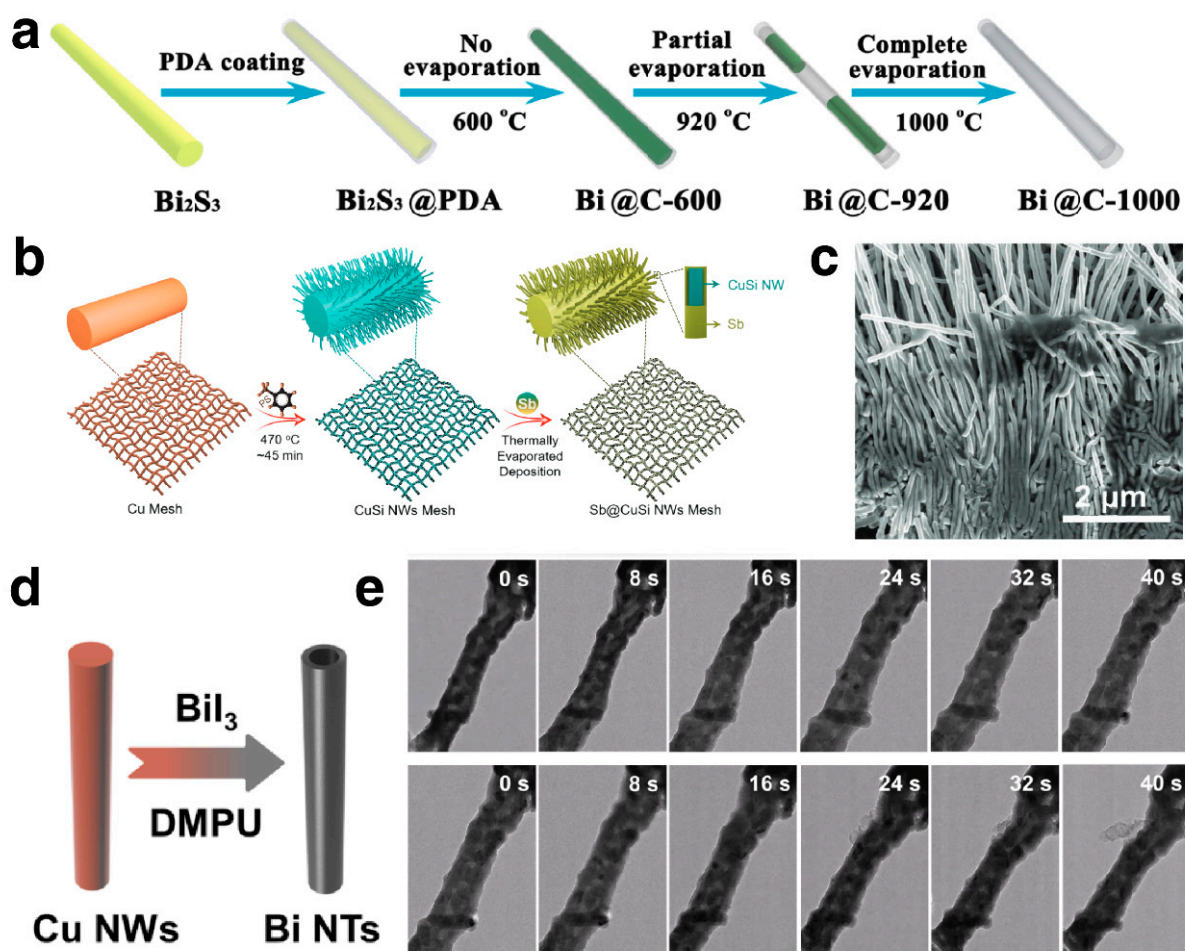
Figure 6. (**a**) The synthesis illustration of process of the Bi@C. Reproduced with permission [81]. Copyright 2020, Elsevier. (**b**) Schematic illustration of the synthesis of the Sb@CuSi NWs; (**c**) the SEM image of the Sb@CuSi NWs. Reproduced with permission [82]. Copyright 2023, Wiley-VCH. (**d**) Schematic illustration of the synthesis of the Bi NTs. (**e**) In situ TEM analysis of the Bi NTs. Reproduced with permission [83]. Copyright 2022, American Chemical Society.

In fact, for metallic anodes such as Bi, Sn and Sb, the carbon modification is sometimes not indispensable. Imtiaz et al. directly deposited Sb on the $Cu_{15}Si_4$ nanowires, which have a strong anchoring effect for Sb (Figure 6b) [82]. The nanowires with an average diameter of 99 nm and length of several micrometers are arranged regularly on the Cu mesh (Figure 6c). The spaces between nanowires can act as a buffer zone for Sb expansion during potassiation. With iodine ion assistance, Bi nanotubes were fabricated via galvanic replacement (Figure 6d) [83]. Due to the metallicity of Bi, the cross-arranged Bi nanotubes can construct electron transport networks and the 1D nanostructure and void of nanotubes can effectively release the volumetric stress during sodiation. As shown in Figure 6e, the in situ TEM observation reveals that the Bi nanotubes expand along the inside and outside of the tube wall, demonstrating the structural robustness during sodiation and desodiation.

Apart from the typical 1D structures mentioned above, some structural designs on nanoarrays are also classified as 1D materials. In 2020, inspired by durian, triangular pyramid arrays of $Bi_{0.75}Sb_{0.25}$ were fabricated on Cu substrates with appreciable electrochemical robustness when used as anode for SIBs. (Figure 7a,b) [43]. Finite-element analysis was employed to reveal the electric field distribution and Na^+ ion concentration during electrochemical reactions. As shown in Figure 7c, the electric field is concentrated at the tip, which would attract Na^+ around the electrode and lead to ion enrichment. Based on this nanostructure, the electrode reaction kinetics are promoted and a Na^+ supply at

high current density is guaranteed. Based on similar design ideas, SbSn alloy nanoarrays were fabricated on Cu substrates, which possess a triangular pyramid-like structure (Figure 7d,e) [84]. Finite-element modeling reveals that the top end is conducive to the efficient usage of the active material and the relief of the inner stress during sodiation. Based on the aforementioned work, 1D materials can effectively buffer the volume expansion and provide a fast electric and ionic pathway, leading to enhanced electrochemical performance.
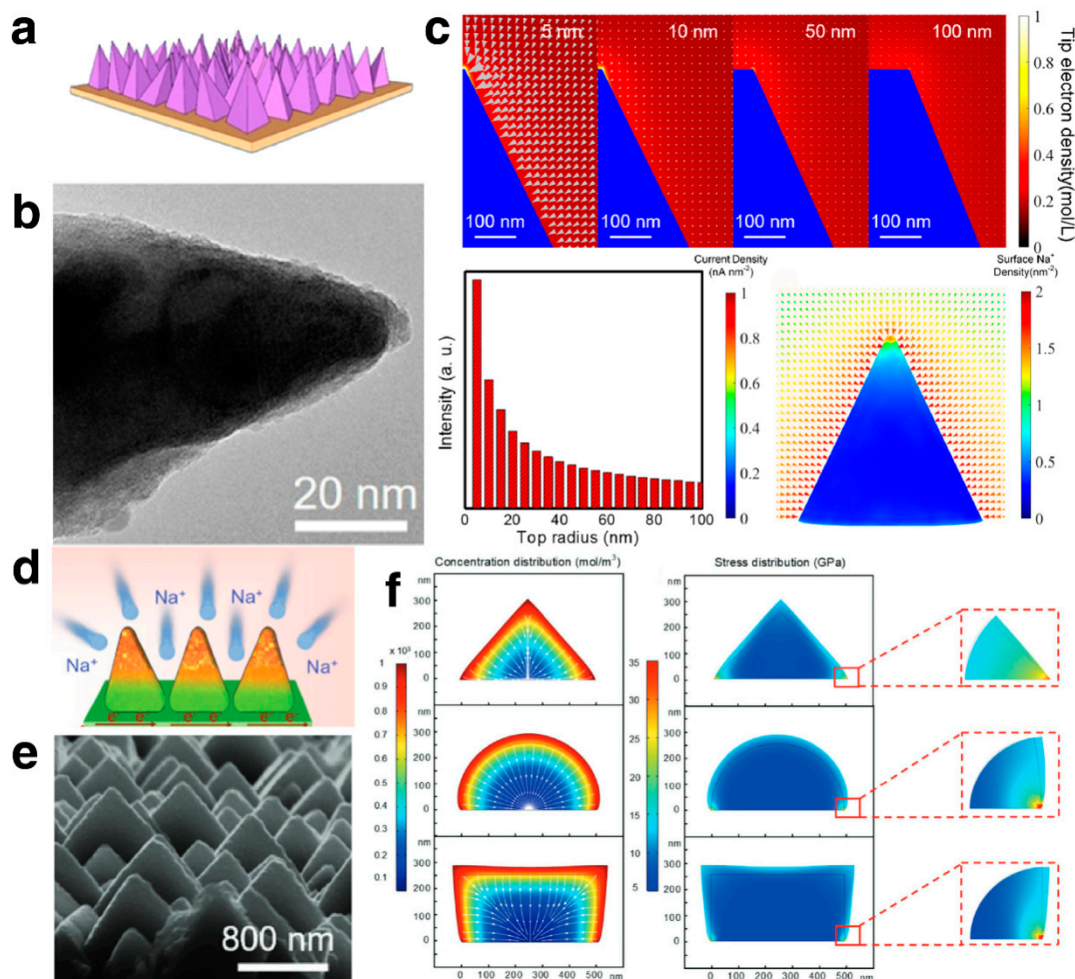

Figure 7. (**a**,**b**) Schematic illustration and TEM images of the $Bi_{0.75}Sb_{0.25}$ array; (**c**) finite-element analysis of the $Bi_{0.75}Sb_{0.25}$ anode. Reproduced with permission [43]. Copyright 2020, American Chemical Society. (**d**,**e**) Schematic illustration and SEM images of the SbSn array; (**f**) finite-element simulation of the SbSn anode. Reproduced with permission [84]. Copyright 2021, Wiley-VCH.

3.3. 2D Materials: Nanosheets, Nanoslices

Two-dimensional materials refer to materials with small sizes in one dimension and relatively large scales in the other two dimensions. Since the discovery of graphene in 2004, 2D materials have entered a period of rapid development owing to their unique physicochemical properties. In addition, owing to their high intrinsic charge carrier mobilities, mechanical robustness and superior flexibility, 2D materials and 2D structure design methodologies are widely used in the development of alloy-type anodes for SIBs and PIBs. During the alloy and dealloy reaction process, 2D materials can also provide short ion diffusion paths and release the stress changes in the normal direction. Based on the metallicity of alloy-type elements or incorporating with carbon materials, fast electron transfer is guaranteed, leading to enhanced electrochemical performance. Reviewing recent

investigations on the alloy-type anode materials for SIBs and PIBs, extensive effort has been devoted to robust structures and fast reaction kinetics [85].

As mentioned before, among the many allotropes of phosphorus, BP has a layered crystal structure and high electrical conductivity. In the BP crystal structure, atoms are strongly bonded in the plane, forming layers, and the layers are stacked through van der Waals forces [86]. It is worth noting that the monolayer of BP, also called phosphorene, has unique physical and chemical properties. In 2014, phosphorene was fabricated via the sticky tape technique, which is the same as that found for graphene [87,88]. Therefore, the 2D structural designs of the P-based anode mainly focus on BP and the corresponding phosphorene. In 2015, Sun et al. fabricated the composite with few phosphorene layers sandwiched between graphene layers [89]. Figure 8a shows a schematic illustration of the crystal structure and the sodiation process of the BP. The sandwich structure was confirmed by high-resolution TEM imaging (Figure 8b). Combining the in situ TEM and ex situ XRD techniques, the sodiation mechanism of the BP was revealed as a two-step reaction process, including the intercalation of Na^+ and the following alloy reaction to Na_3P. The 2D sandwich structure shows a high specific capacity of 2440 mAh g^{-1} after cycling at 0.05 A g^{-1} for 100 cycles. In the robust structure, graphene layers play a vital role in the mechanical strength and electrical transfer and the layer-by-layer structure can accommodate the anisotropic expansion of phosphorene. Furthermore, this design idea is inherited and improved, and achieves better performance. Shuai et al. developed a sandwich-structured phosphorene–graphene hybrid via electrochemical exfoliation and the solvothermal process, which delivered excellent cycling performance (1582.6 and 1120.6 mAh g^{-1} after 200 cycles at 1 and 5 A g^{-1}, respectively) [90].
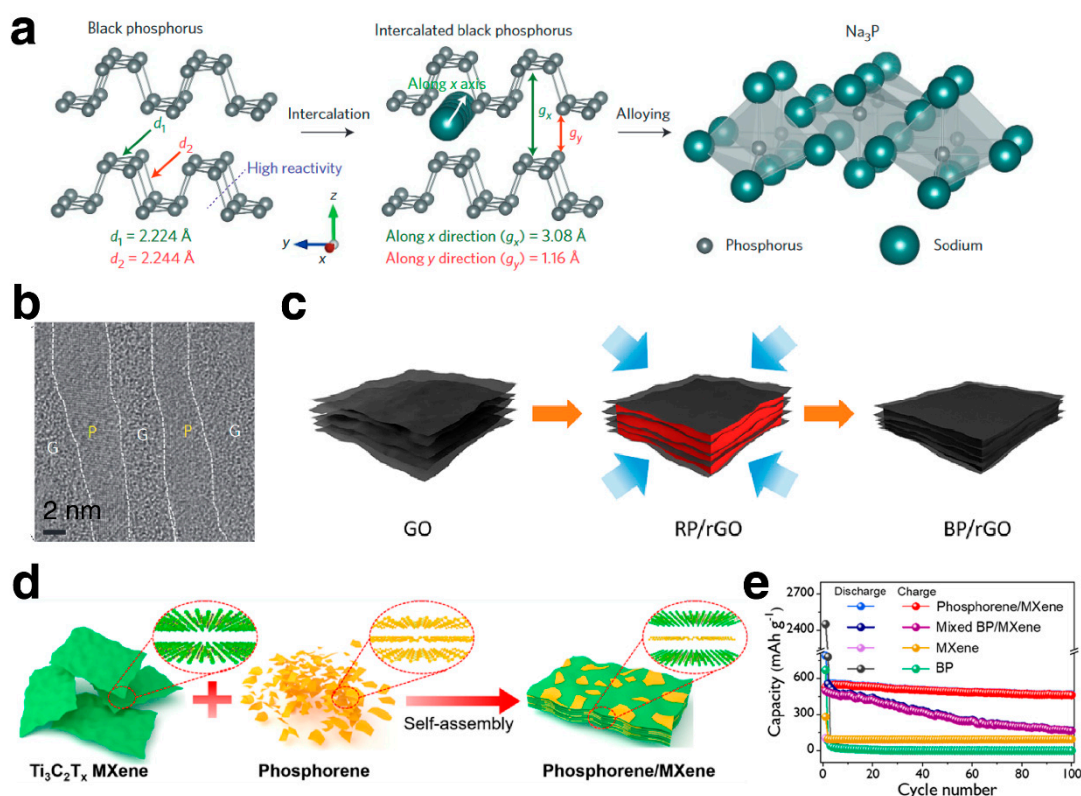
Figure 8. (**a**) Schematic illustration of the BP and the sodiation process; (**b**) HRTEM image of the cross-section of the phosphorene–graphene hybrid. Reproduced with permission [89]. Copyright 2015, Nature Publishing Group. (**c**) Schematic illustration of the BP/rGO. Reproduced with permission [42]. Copyright 2018, American Chemical Society. (**d**) Schematic illustration of the synthetic processes for phosphorene/MXene hybrid structure; (**e**) the cycling performance of the phosphorene/MXene. Reproduced with permission [91]. Copyright 2020, American Chemical Society.

Liu et al. applied a pressure of 8 GPa on the RP/rGO, inducing the transformation of RP to BP at room temperature, as shown in Figure 8c [42]. The freestanding P-based anode delivers a capacity of 1250 and 640 mAh/g after 500 cycles at 1 and 40 A/g, respectively. Similar to graphene, MXene is a new family of 2D transition-metal carbides and/or nitrides with high electronic conductivity and good elastic properties. Guo et al. fabricated the phosphorene/MXene hybrid anode, as shown in Figure 8d [91]. The in-depth XPS revealed the fluorine-rich SEI formed by the fluorine terminations of the MXene, which can effectively improve the Coulombic efficiencies and cycling performance of the phosphorene/MXene anodes. Based on the well-designed nanostructure, the composites delivered enhanced electrochemical performance with 535 mAh g^{-1} at 0.1 A g^{-1} (Figure 8e). In addition to BP, blue phosphorus also has a layered crystal structure and similar physical and chemical properties [92]. Based on the first-principles calculations, Fan et al. investigated the graphene/blue-phosphorus heterostructure and its application for SIBs, which shows that the graphene can dramatically enhance the Na adsorption process [93]. As mentioned above, conductive 2D materials can maximize the advantages of the high capacity of the P-based anode.

Since the report of phosphorene, a considerable amount of research interest has been devoted to the 2D materials of elements in the VA group. As mentioned above, the crystal structures of Sb and Bi exhibit a typical layered feature, which is promising in developing ultrathin 2D nanomaterials. In recent years, many kinds of 2D structure of Sb and Bi have been constructed to improve the electrochemical performance in SIBs and PIBs, including ultrathin nanosheets, hierarchical nanosheets, nanoflower, etc. The 2D antimonene can be fabricated via liquid-phase exfoliation [94], mechanical exfoliation [95] and van der Waals epitaxy [96,97]. Tian et al. acquired few-layer antimonene (FLA) via the liquid-phase exfoliation of β-antimony without any surfactant, as shown in Figure 9a [56]. The atomic force microscopy (AFM) results show that the thickness of the as-synthesized FLA is about 7 nm. The in situ XRD characterization demonstrates that the 2D Sb nanosheets undergo anisotropic volume expansion and the phase evolution mechanism during cycling. The theoretical calculation reveals that the 2D FLA has a very low diffusion barrier for Na⁺. After evaluation in SIBs, the FLA delivered a high rate capability (with capacity retention of 429 mAh g^{-1} at 5 C) and long cycle stability (620 mAh g^{-1} after 150th cycles at 0.5 C with capacity retention ratio of 99.7%) (Figure 9b,c). To achieve an excellent K-storage performance of bismuth-based anode materials in PIBs, Shen et al. developed bismuthine nanosheets (FBNs) via the insertion of tetraheptylammonium cations into the bulk bismuth followed by ultrasonication assisted by an external forcefield (Figure 9d) [57]. The AFM image shows that the thickness of the ultrathin bismuthene nanosheets is about 1.3 nm, suggesting that the FBNs are dominantly constructed by two bismuthine layers. When used as the anode for PIBs, the FBNs remained above 200 mAh g^{-1} even after cycling over 2500 cycles at a high current density of 20 A g^{-1}, suggesting a stable nanostructure and highly reversible potassiation process. Except for ultrathin bismuthene, hierarchical bismuth nanosheets (2D-Bi) can also provide superior potassium storage performance with an even better rate capability. Through the simple reduction reaction with zinc powder, the 2D-Bi was obtained, as shown in Figure 9f. Compared with other types of bismuth-based materials, including 0D-Bi, 1D-Bi and 3D-Bi, the 2D-Bi delivered the best rate performance (with a capacity retention of 345 mAh g^{-1} at 30 A g^{-1}) and cycle stability (Figure 9g). To investigate the reason, Cheng et al. tested its morphology after cycling and found that the 2D-Bi evolved into a stable two-dimensional network structure after cycling. This report reveals similar patterns to previous reports on phosphorene. In 2019, Liu et al. prepared holey phosphorene via an electrochemical assistance method [98]. Typically, the BP was used to assemble a sodium-ion battery. After discharging, the coin cell was disassembled and holey phosphorene was obtained after washing and sonication. Therefore, the reaction mechanism of two-dimensional materials in batteries remains to be further determined. Owing to the unique physical and chemical properties, the 2D Bi and Sb nanostructures were used in other electrochemical applications [99–103]. Therefore, the study of two-

dimensional Bi/Sb-based materials is quite important for promoting the development of alkalic ion batteries and other electrochemistry fields.
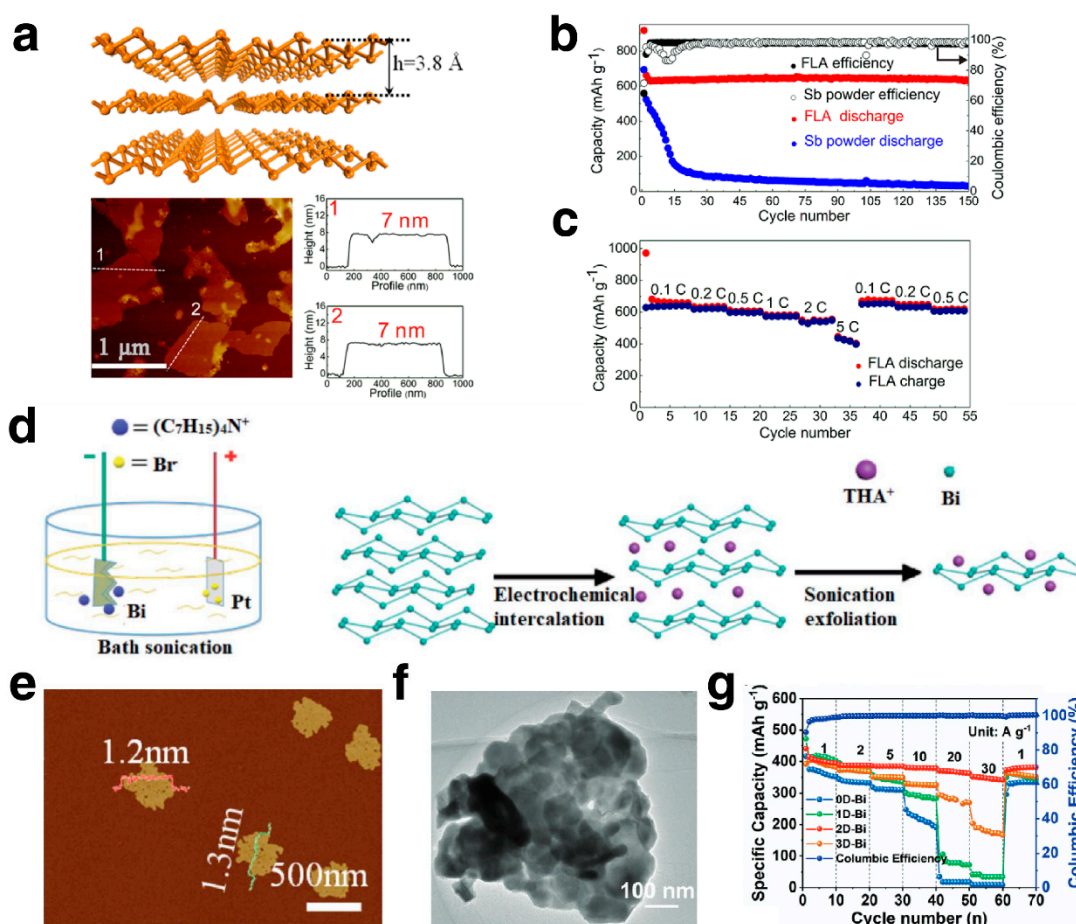

Figure 9. (**a**) Crystal structure, AFM image and corresponding profile terraces of the FLA; (**b**,**c**) electrochemical performance of the FLA and Sb powder. Reproduced with permission [56]. Copyright 2018, American Chemical Society. (**d**) Schematic illustration of the fabrication of FBN via electrochemical exfoliation; (**e**) AFM image of the FBNs. Reproduced with permission [57]. Copyright 2020, The Royal Society of Chemistry. (**f**,**g**) Morphology and the rate capability of 2D-Bi. Reproduced with permission [47]. Copyright 2021, Wiley-VCH.

3.4. 3D Materials: Nanoframeworks, Porous Structure

Three-dimensional materials are defined as materials with large scale in all three dimensions. In terms of the nanomaterial structure, 3D materials usually have unique substructures. Reviewing the structural design of anode materials, the transport process of electrons and ions is a key step in the electrochemical reaction. In other words, a suitable electrode structure should enable the rapid transport of electrons and ions. For alloy-type materials, sufficient pores need to be reserved to alleviate volume expansion. Therefore, a suitable electrode material needs to possess some unique structural characterizations, including a high specific surface area, continuous pore structure for ionic transport, high conductivity and robust mechanical strength for electron transfer and stable cycling. Therefore, compared with 0D/1D/2D materials, 3D materials can achieve a 3D conductive skeleton and structural mechanical stability through unique structural design, thereby eliminating the need for the introduction of carbon modifications.

As mentioned above, the storage performance of the RP was restricted by the large volume expansion and the consequent electrode pulverization. To address these issues, a micron-sized red phosphorus with an abundant pore structure (HPRP) was fabricated

via the hydrothermal method for high-performance lithium storage (Figure 10a–c) [44]. In this work, the porous nanostructure of the HPRP can effectively accommodate the expansion and offer fast ion transport and good structural robustness, leading to superior electrochemical performance in LIBs. Such a creative structure can provide guidance for the design of anode electrode materials for SIBs and PIBs. It is worth noting that the P-based anode still suffers from low electrical conductivity in addition to the high volume expansion. Therefore, appropriate conductive skeleton should be introduced into the nanostructure. In 2021, Liu et al. developed a Sb-doped RP/carbon anode with Ketjenblack and a multiwalled CNT forming the conductive framework (Figure 10d) [104]. The micrometer-sized particles were made up of nanometer-sized secondary-like particles. The unique 3D structure effectively accommodates the mechanical stress and restrains the decomposition of the electrolyte, leading to an initial Coulombic efficiency up to about 90% (Figure 10e). In addition, in situ SEM and XPS confirmed the high reversibility of the structure during sodiation and desodiation. Likewise, out of consideration of improving electronic conductance and buffering the volume expansion, Liu et al. proposed encapsulating RP into networked carbon nanocages (RP@CNCs) based on the phosphorus-amine-based method (Figure 10f,g) [105]. The carbon nanocages play the role of conductive frameworks and buffer the volume expansion of RP. When used as an anode for SIBs, the RP@CNCs delivers a high-rate capability and excellent long-cycling performance with a capacity retention ratio of over 80% after 1300 cycles at 5 A g^{-1} (Figure 10h,i). To sum up, 3D materials with a conductive framework and appropriate pore structure can generate a high electrochemical performance of P-based materials for Na/K storage.

Recently, much creative investigation has been carried out about the 3D nanostructure of the Sn/Sb/Bi-based anode. In 2017, Wang et al. investigated bulk Bi as the anode material of SIBs (Figure 11a) [106]. Unlike previous reports operating in ester electrolytes, bulk bismuth gradually evolved into 3D porous nanostructures during the cycling process in ether electrolytes, as shown in Figure 11b. The bulk Bi delivers a good rate capability with 356 mAh g^{-1} at 2 A g^{-1} and stable cycling performance with only 5.6% of attenuation after 2000 cycles (Figure 11c). Afterwards, Cheng and coworkers directly synthesized 3D continuous bulk porous bismuth via a facile reduction reaction in an aqueous system (Figure 11d) [46]. The 3DPBi-based anode for SIBs showed an unprecedented rate capability with only 4.4% of attenuation at 60 A g^{-1}. The in situ TEM characterization revealed that the 3D continuous porous structure can effectively buffer the volume expansion during sodiation. Owing to the stable nanostructure, the 3DPBi maintains a bicontinuous structure of electrons and ions during repeated cycling, ensuring the rapid progress of electrochemical reactions (Figure 11e). Even though porous bismuth nanomaterials can meet the high electronic conductivity through the structural design, carbon modification can further improve the lifespan of Bi-based anode materials. Afterwards, porous bulk bismuth with carbon modification (P-Bi/C) was fabricated via the magnesiothermic reduction of $(BiO)_2CO_3$ (Figure 11f). The stable nanostructure can deliver an ultralong cycling life for over 20,000 cycles (Figure 11g). Except for the unique advantages of the 3D porous structure, the carbon layer modification induces a more appropriate SEI structure with the organic species in the outer layer and the inorganic species in the inner layer, as shown in Figure 11h. Therefore, the 3D structure with an abundant porous reservation can provide robust nanoligaments and electric conductive frameworks, which result in fast electrochemical kinetics and excellent structural stability.
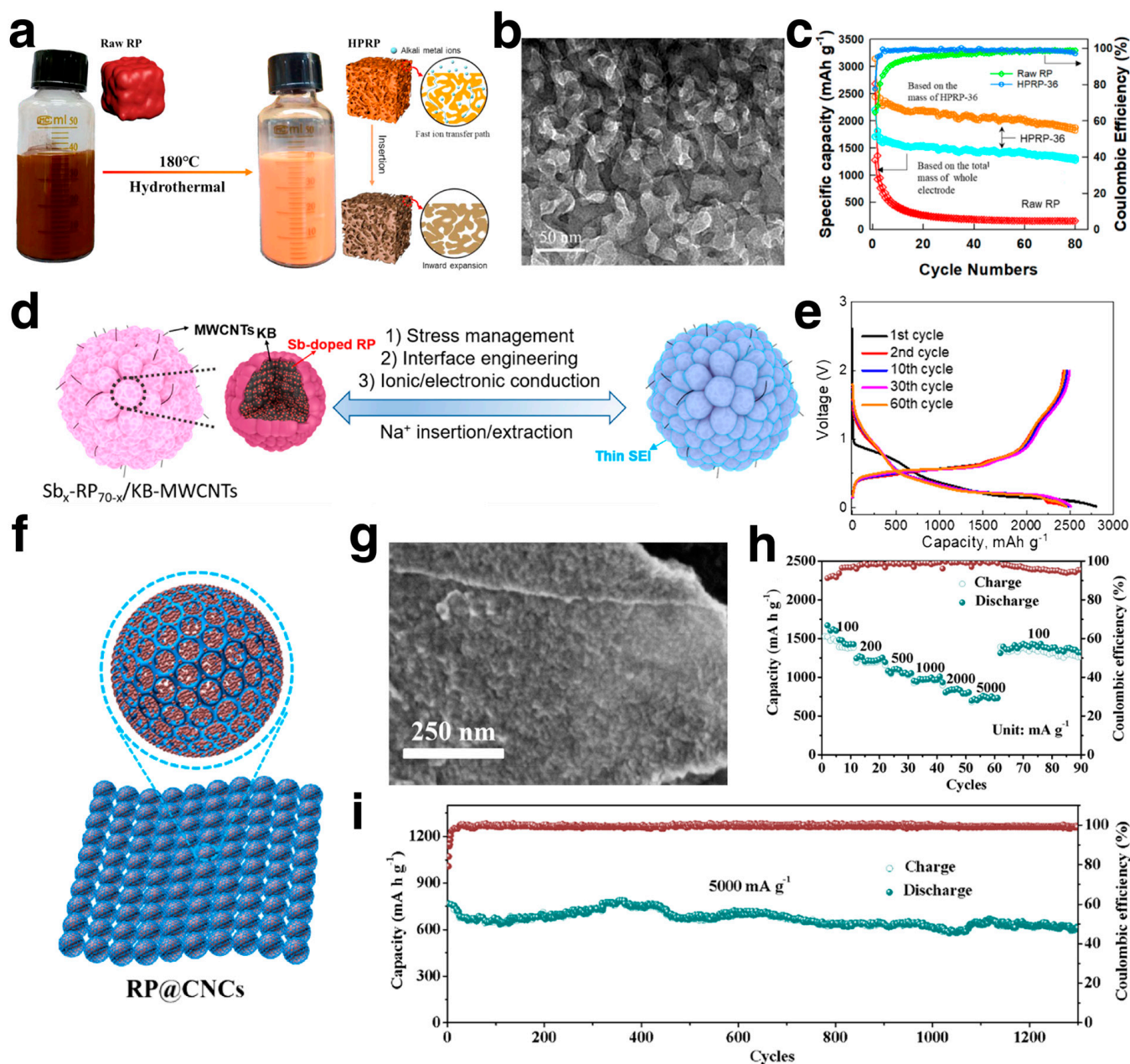
Figure 10. (**a–c**) Schematic illustration of synthesis, morphology and cycling performance of the HPRP. Reproduced with permission [44]. Copyright 2021, American Chemical Society. (**d,e**) Schematic illustration and electrochemical performance of the $Sb_x\text{-}RP_{70-x}/C_{30}$ composite. Reproduced with permission [104]. Copyright 2021, American Chemical Society. (**f–i**) Schematic illustration, morphology and electrochemical performance of the RP@CNC composite. Reproduced with permission [105]. Copyright 2021, American Chemical Society.
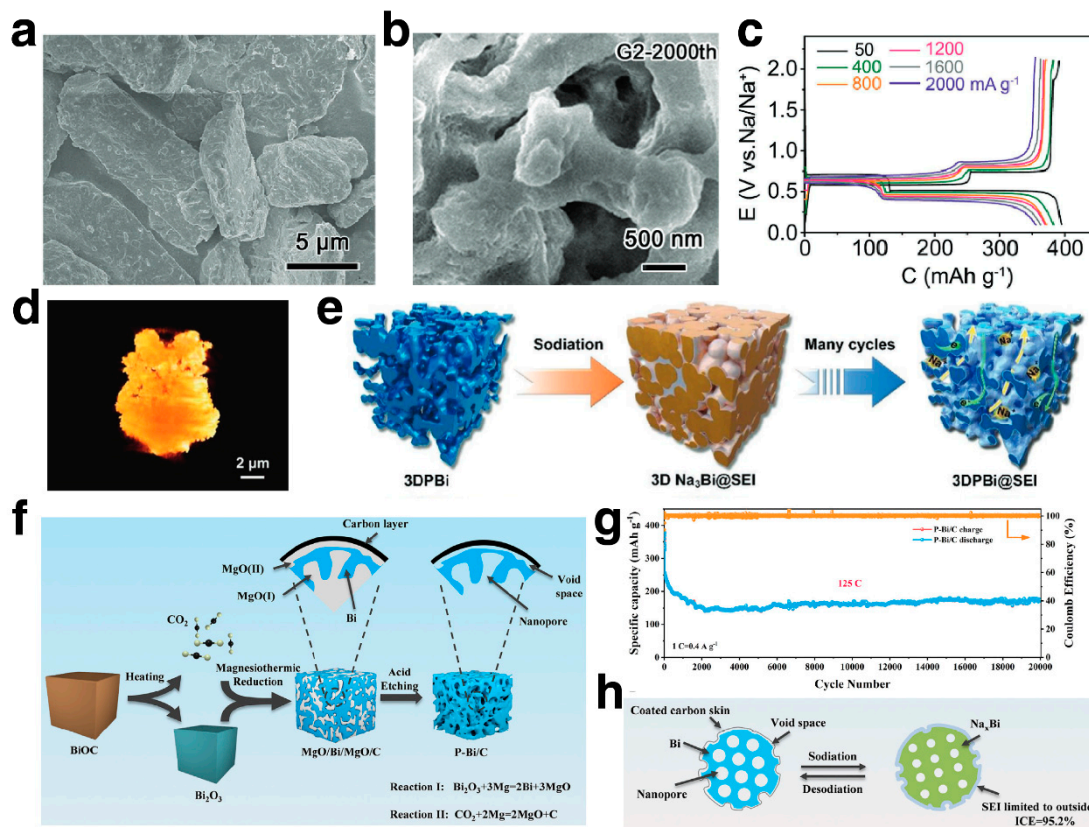
Figure 11. (**a**,**b**) SEM images of the bulk Bi and the electrode after 2000 cycles in ether electrolyte; (**c**) rate performance of the bulk Bi [106]. Reproduced with permission. Copyright 2017, Wiley-VCH. (**d**,**e**) Three-dimensional reconstruction imaging and cycling process of the 3DPBi. Reproduced with permission [46]. Copyright 2021, Wiley-VCH. (**f**–**h**) Synthesis schematic illustration, electrochemical performance and the sodiation process of P-Bi/C composite. Reproduced with permission [107]. Copyright 2023, Elsevier.

As for Sb, Sn and some binary alloy materials, the 3D structure design can also dramatically improve the electrochemical performance for SIBs and PIBs. As an effective method, dealloying has been used to fabricate nanomaterials with unique 3D structures. In 2018, nanoporous Sb (NP-Sb) was synthesized by evaporating the Zn in the ZnSb alloy under vacuum conditions [108]. The porous structure of NP-Sb can be adjusted by the proportion of pristine ZnSb alloy, as shown in Figure 12a. The nanostructure of NP-Sb prepared by the Zn-Sb alloy with a Zn-to-Sb ratio of 4:1 is shown in Figure 12b. Through adjusting the ingredient ratio in the ZnSb alloy, the porous structure can be easily changed. When the antimony content in the alloy is reduced to 20%, the NP-Sb-20 delivers an outstanding rate performance for potassium storage, as shown in Figure 12c. Also based on the dealloying reaction, nanoporous Bi-Sb alloys were also fabricated [109]. The structure of the Bi-Sb alloy is also durable by adjusting the element ratio of the ternary Mg-based precursors. As shown in Figure 12d,e, the Bi-Sb alloy is composed by nanoligaments with a diameter of about 30 nm and abundant nanopores. Owing to the unique 3D framework and short diffusion path of Na$^+$, the BiSb alloy shows outstanding rate performance (Figure 12f). Except for dealloying methods, Wang et al. proposed the triggering of the electrostatic displacement reaction between Cu and Sn^{2+} by introducing thiourea as a ligand and fabricated 3D porous Sn on Cu foil via the electrostatic displacement reaction (Figure 12g,h), which also delivers good electrochemical performance for sodium storage. As mentioned above, there are various synthesis methods for developing 3D nanostructures of the alloy-type anode materials. The 3D structure has various shape details, and its void structure can be regulated via various methods to achieve demanding requirements under working conditions. In addition, 3D

nanostructures of the alloy-based anode are conducive to improving the energy density and area-specific volume, due to the high proportion of active substances.
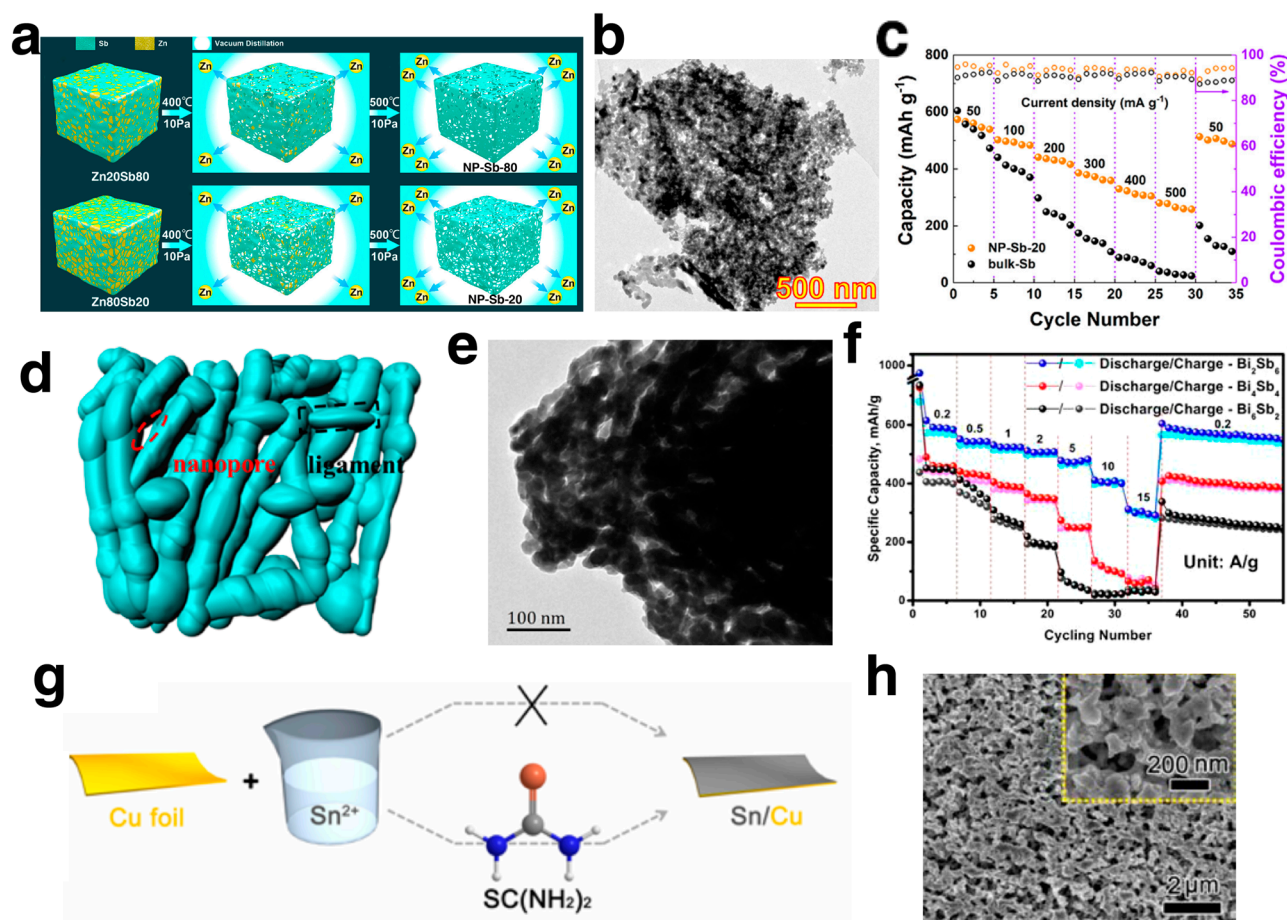

Figure 12. (**a**) Schematic illustration of the NP-Sb synthesis process via dealloying process of Zn20Sb80 and Zn80Sb20; (**b**,**c**) TEM image and the rate performance of the NP-Sb-20. Reproduced with permission [108]. Copyright 2018, American Chemical Society. (**d**–**f**) Schematic illustration, TEM image and rate performance of the np-Bi-Sb alloys. Reproduced with permission [109]. Copyright 2018, American Chemical Society. (**g**,**h**) Synthesis process and morphology of the Sn/Cu. Reproduced with permission [110]. Copyright 2018, Wiley-VCH.

4. Summary and Outlook

In this review, we comprehensively summarized recent advances in alloy-type anodes for SIBs and PIBs. The nanostructure design of alloy-type anode materials, especially the nanosized, low-dimensional structures and some special nanostructure designs, were emphasized. Based on the unique structures, the dependency of structure and electrochemical performance was focused on. According to the dimensionality, the nanostructures of the alloy-type anodes were classified into 0D, 1D, 2D and 3D. Although based on different structural design ideas, in response to the inherent defects of alloy-type anode materials such as the high volume expansion and low electronic conductivity of certain elements, researchers have continuously achieved high electrochemical performance for sodium and potassium storage through improving electronic and ionic conductivity, enhancing the mechanical properties and tuning the stress distribution. For a more intuitive comparison, we summarize the synthesis methods and electrochemical performance of the various alloy-type anodes for SIBs and PIBs in Tables 2–5. However, although the performance of alloy-based anodes has made tremendous progress under laboratory conditions, there is

still a long way to go for industrial applications. To meet the requirements for industry application, some key issues should be addressed in future investigations.

Table 2. Synthesis methods and electrochemical performance of P-based anode with different dimensional structures for SIBs and PIBs.

Dimensional Structure	Materials	Synthesis Methods	Electrolytes	ICE (%)	Cycling Performance [a]	Rate Capability [b]	Refs.
0D	P@TBMC	vaporization–condensation-conversion	1 M $NaClO_4$ in EC/DEC with 5% FEC	69.8	580/800th/2.5	430/8	[62]
	HHPCNSs/P	vaporization–condensation process	1 M $NaClO_4$ in EC/DEC	75.1	861.8/1000th/5	831.1/10	[111]
	red P@N-PCT	vaporization–condensation method	1 M $NaClO_4$ in EC/DMC with 5% FEC	-	1157/100th/2	572/10	[112]
	P/TiN/Gnps	mechanical milling method	1 M $NaClO_4$ in EC/DEC with 5% FEC	86.8	91.3%/300th/0.2	339/20	[113]
	NRP−rGO	phosphorus-amine-based method	1 M $NaClO_4$ in EC/DEC with 10% FEC	61.2	390/5000th/5	718/5	[59]
	RP@BP/3DNG	solvothermal treatment	1 M $NaClO_4$ in EC/DMC with 5% FEC	65.3	465.5/1200th/10	521.3/10	[61]
	P/C	evaporation–condensation method	1 M KFSI in EC/DEC	58.8	212/10,000th/3.2	287/11.2	[51]
	P@TBMC	vaporization–condensation-conversion	0.6 M KPF_6 in EC/PC	63.5	244/200th/0.5	136/2	[62]
	red P@CN	vaporization–condensation strategy	0.8 M KPF_6 in EC/DEC	59	427.4/40th/0.1	323.7/2	[55]
1D	P_{red}@CNF	vaporization–condensation method	1 M $NaPF_6$ in EC/DEC	-	1850/500th/0.1	-	[80]
	vf2-P	selenium-induced method	1 M $NaClO_4$ in EC/PC with 5% FEC	89.7	1785/2800th/1 C	1190/25 C	[50]
2D	phosphorene-graphene	self-assembly	1 M $NaPF_6$ in EC/DEC with 10% FEC	~80	2440/100th/0.05	-	[89]
	BP/rGO	pressure synthesis	1 M $NaClO_4$ in DMC with 10% FEC	89.5	1250/500th/1	720.8/40	[42]
	phosphorene–graphene	electrochemically exfoliated and solution method	1 M $NaClO_4$ in PC with 5% FEC	80.6	1582.6/200th/1	1499/5	[90]
	phosphorene/MXene	self-assembly	1 M $NaClO_4$ in EC/PC	63.1	340/1000th/1	193/5	[91]
3D	NPRP@RGO	boiling	1 M $NaClO_4$ in PC with 5% FEC	78.5	1250/150th/0.17	657/3.47	[114]
	RP@CNCs	evacuation-filling process	1 M $NaClO_4$ in EC/DEC with 10% FEC	-	1363/150th/0.1	750/5	[105]
	Sb_7-RP_{63}/C_{30}	high-energy ball milling process	1 M $NaPF_6$ in PC with 2% FEC	88	2356/70th/C/3	1779/2C	[104]
	HPRP@Bi	hydrothermal and self-limited growth	4 M KFSI in DME	43.9	283/200th/0.05	106.4/3	[115]

[a] The data were registered by specific capacity (mAh g^{-1})/cycle number (n)/current density (A g^{-1}); [b] the data were registered by specific capacity (mAh g^{-1})/current density (A g^{-1}).

Table 3. Synthesis methods and electrochemical performance of Sn-based anode with different dimensional structures for SIBs and PIBs.

Dimensional Structure	Materials	Synthesis Methods	Electrolytes	ICE (%)	Cycling Performance [a]	Rate Capability [b]	Refs.
0D	8-Sn@C	aerosol spray pyrolysis method	1 M NaClO$_4$ in EC/DEC	67	415/500th/1	349/4	[116]
	PCNCs-Sn	template-assisted CVD and in situ reduction	1 M NaClO$_4$ in EC/PC with 5% FEC	73	202/550th/1.28	188/2.56	[117]
	Sn@CFC	electrospinning method	1 M NaClO$_4$ in EC/DMC with 5% FEC	42.3	255/200th/0.05	100/1	[118]
1D	Sn@NC	annealing	1 M NaPF$_6$ in DME	78.4	347/10,000th/5	437/5	[119]
	Sn nanofibers	electrodeposition	1 M NaClO$_4$ in PC with 2% FEC	68	776/100th/0.1C	~260/5C	[120]
3D	porous Sn	replacement reaction	1 M NaPF$_6$ in DME	-	660/400th/2.5	667.6/6.5	[110]
	α-Sn	Commercial	1 M NaPF$_6$ in DGM	80	451/3500th/2	464/4	[121]

[a] The data were registered by specific capacity (mAh g^{-1})/cycle number (n)/current density (A g^{-1}); [b] the data were registered by specific capacity (mAh g^{-1})/current density (A g^{-1}).

Table 4. Synthesis methods and electrochemical performance of Sb-based anode with different dimensional structures for SIBs and PIBs.

Dimensional Structure	Materials	Synthesis Methods	Electrolytes	ICE (%)	Cycling Performance [a]	Rate Capability [b]	Refs.
0D	Sb@NS-3DPC	pyrolysis	1 M NaClO$_4$ in PC with 10% FEC	61.1	259/20000th/10	283.8/10	[73]
	carbon-coated Sb/MXene	calcination	5 M KFSI in DME	76.7	216/1200th/0.5	212/2	[48]
	Sb@CSN	electrospray-assisted strategy	4 M KTFSI in EC/DEC	61	504/220th/0.2	530/0.2	[72]
	Sb@CNFs	carbon-thermal reduction	2 M KFSI in DME	47	338/200th/0.2	121/2	[74]
1D	Bi$_{0.75}$Sb$_{0.25}$ pyramid arrays	electrodeposition and annealing	1 M NaPF$_6$ in DME	86	284/2000th/0.5	335/2.5	[43]
	SbSn nanoarrays	electrodeposition and annealing	1 M NaPF$_6$ in DME	83	511/800th/2C	521/5C	[84]
	Sb@Cu$_{15}$Si$_4$ NW array	thermal deposition	4 M KFSI in DME	-	250/1250th/0.2	228.4/2	[82]
2D	few-layer antimonene	liquid-phase exfoliation	1 M NaClO$_4$ in EC/DEC with 5% FEC	64.7	620/150th/0.5C	429/5C	[56]
	antimonene/C	liquid-phase exfoliation	1 M NaPF$_6$ in EC/DMC with 5% FEC	71.2	451.3/150th/0.2	334.5/5	[100]
3D	np-Bi$_2$Sb$_6$	dealloying	1 M NaPF$_6$ in PC with 5% FEC	69.8	258/2000th/0.2	304.2/15	[109]
	NP-Sb	dealloying	0.8 M KPF$_6$ in EC/DEC	-	318/50th/0.1	265/0.5	[108]
	Microsized Sb	commercial	4 M KFSI in DME	74.2	553/200th/0.2	305/3	[122]

[a] The data were registered by specific capacity (mAh g^{-1})/cycle number (n)/current density (A g^{-1}); [b] the data were registered by specific capacity (mAh g^{-1})/current density (A g^{-1}).

Table 5. Synthesis methods and electrochemical performance of Bi-based anode with different dimensional structures for SIBs and PIBs.

Dimensional Structure	Materials	Synthesis Methods	Electrolytes	ICE (%)	Cycling Performance [a]	Rate Capability [b]	Refs.
0D	Bi@C composite	annealing	1 M NaPF$_6$ in DME	50.3	265/30,000th/8	232/60	[45]
	Bi@N-C	annealing	1 M NaPF$_6$ in DME	36.5	235/2000th/10	152/100	[123]
	BiSb@C composite	annealing	5 M KFSI in DME	70.2	~330/600th/0.5	152/2	[65]
	BiND/G	in situ reduction	1 M KPF$_6$ in DME	78	213/500th/5	215/10	[64]
1D	Bi NTs	iodine-ion-assisted galvanic replacement	1 M NaPF$_6$ in DME	69.2	355/15,000th/20	319/150	[83]
	BNW@G film	vacuum filtration assembly	1 M NaPF$_6$ in DME	82.7	276/1000th/1	295/5	[53]
2D	Bi@NC	solvothermal and carbonization	1 M NaPF$_6$ in DME	85.1	~325/5000th/10	341.5/10	[103]
	2D-Bi	solution synthesis method	1 M KPF$_6$ in DME	89.2	344/750th/10	345/30	[47]
	FBNs	electrochemical exfoliation	1 M KPF$_6$ in DME	-	200/1500th/20	182/20	[57]
3D	Bulk Bi	commercial	1 M NaPF$_6$ in G2	94.8	389/2000th/0.4	356/2	[106]
	3DPBi	solution reduction	1 M NaPF$_6$ in DME	65.9	374/3000th/10	354/60	[46]
	LC-Bi composite	calcination	1 M NaPF$_6$ in DME	53.4	225.6/2600th/1	236.1/100	[49]
	P-Bi/C	annealing	1 M NaPF$_6$ in DME	95.2	178/20,000th/50	101/72	[107]
	Bulk Bi	commercial	1 M KPF$_6$ in DME	87.2	322.7/300th/0.8	-	[124]

[a] The data were registered by specific capacity (mAh g^{-1})/cycle number (n)/current density (A g^{-1}); [b] the data were registered by specific capacity (mAh g^{-1})/current density (A g^{-1}).

(1) Most of the reported improved electrochemical performance was evaluated based on the specific capacity under laboratory conditions with low mass loading and tap density. One of the main competitive points of alloy-type anode materials is the high volumetric energy density. In a large number of studies, the introduction of porous carbon materials and some inactive materials inevitably reduces the energy density of materials. Therefore, in order to obtain higher energy density, the content of active substances in composite materials needs to be increased and the porous structure of the material needs to be designed more precisely. In addition, the electrochemical performance of high-loading electrodes is often overlooked in laboratory investigation. In order to meet the requirements of industrial applications, it is necessary to optimize the high loading performance of the anode materials and solve related technical issues.

(2) The coulombic efficiency, especially the initial coulombic efficiency (ICE), is quite important in the industrial application of SIBs and PIBs. For alloy-type anodes, the low ICEs limit their practical application. Every coin has two sides. Although low-dimensional nanostructures and porous carbon modification with large specific areas can accelerate the reaction kinetics and enhance the electrochemical performance, it will also cause many more side reactions and generate more SEI films, leading to lower ICEs. To tackle this issue, such strategies could be taken into consideration as interfacial engineering and appropriate electrolyte additives, balancing the nanostructure and electrochemical performance.

(3) The morphology evolution mechanisms of the alloy-type anode materials still have to be uncovered. As mentioned above, porous phosphorus nanosheets can be obtained by treating the sodiated BP. The hierarchical bismuth nanosheets can evolve into a two-dimensional network structure after cycling. Bulk Bi can evolve into porous Bi. All these phenomena are not well explained and require further exploration. By studying the structure of alloy materials after recycling, and then using it as a guide for structural design, stable nanostructures can be designed.

Author Contributions: X.C. prepared the original manuscript; D.L. edited the figures; Y.J., F.H. and S.L. revised the manuscript. All authors have read and agreed to the published version of the manuscript.

Institutional Review Board Statement: Not applicable.

Informed Consent Statement: Not applicable.

Data Availability Statement: Data are contained within the article.

Conflicts of Interest: The authors declare no conflict of interest.

References

1. Xu, J.; Zhang, J.; Pollard, T.P.; Li, Q.; Tan, S.; Hou, S.; Wan, H.; Chen, F.; He, H.; Hu, E.; et al. Electrolyte Design for Li-Ion Batteries under Extreme Operating Conditions. *Nature* **2023**, *614*, 694–700. [CrossRef] [PubMed]
2. Wang, Y.; Zhang, X.; Li, K.; Zhao, G.; Chen, Z. Perspectives and Challenges for Future Lithium-Ion Battery Control and Management. *eTransportation* **2023**, *18*, 100260. [CrossRef]
3. Zhu, J.; Wang, Y.; Huang, Y.; Bhushan Gopaluni, R.; Cao, Y.; Heere, M.; Mühlbauer, M.J.; Mereacre, L.; Dai, H.; Liu, X.; et al. Data-Driven Capacity Estimation of Commercial Lithium-Ion Batteries from Voltage Relaxation. *Nat. Commun.* **2022**, *13*, 2261. [CrossRef] [PubMed]
4. Li, M.; Lu, J.; Chen, Z.; Amine, K. 30 Years of Lithium-Ion Batteries. *Adv. Mater.* **2018**, *30*, 1800561. [CrossRef] [PubMed]
5. Huang, Z.; Deng, Z.; Zhong, Y.; Xu, M.; Li, S.; Liu, X.; Zhou, Y.; Huang, K.; Shen, Y.; Huang, Y. Progress and Challenges of Prelithiation Technology for Lithium-Ion Battery. *Carbon Energy* **2022**, *4*, 1107–1132. [CrossRef]
6. Du, H.; Kang, Y.; Li, C.; Zhao, Y.; Wozny, J.; Li, T.; Tian, Y.; Lu, J.; Wang, L.; Kang, F.; et al. Easily Recyclable Lithium-Ion Batteries: Recycling-Oriented Cathode Design Using Highly Soluble $LiFeMnPO_4$ with a Water-Soluble Binder. *Battery Energy* **2023**, *2*, 20230011. [CrossRef]
7. Hou, J.; Ma, X.; Fu, J.; Vanaphuti, P.; Yao, Z.; Liu, Y.; Yang, Z.; Wang, Y. A Green Closed-Loop Process for Selective Recycling of Lithium from Spent Lithium-Ion Batteries. *Green Chem.* **2022**, *24*, 7049–7060. [CrossRef]
8. Fornillo, B.; Lampis, A. From the Lithium Triangle to the Latin American Quarry: The Shifting Geographies of de-Fossilisation. *Extr. Ind. Soc.* **2023**, *15*, 101326. [CrossRef]
9. Chen, Y.; Shi, X.; Lu, B.; Zhou, J. Concave Engineering of Hollow Carbon Spheres toward Advanced Anode Material for Sodium/Potassium-Ion Batteries. *Adv. Energy Mater.* **2022**, *12*, 2202851. [CrossRef]
10. Huang, Z.-X.; Gu, Z.-Y.; Heng, Y.-L.; Huixiang Ang, E.; Geng, H.-B.; Wu, X.-L. Advanced Layered Oxide Cathodes for Sodium/Potassium-Ion Batteries: Development, Challenges and Prospects. *Chem. Eng. J.* **2023**, *452*, 139438. [CrossRef]
11. Zhu, Y.; Wang, Y.; Wang, Y.; Xu, T.; Chang, P. Research Progress on Carbon Materials as Negative Electrodes in Sodium- and Potassium-Ion Batteries. *Carbon Energy* **2022**, *4*, 1182–1213. [CrossRef]
12. Hu, J.; Hong, Y.; Guo, M.; Hu, Y.; Tang, W.; Xu, S.; Jia, S.; Wei, B.; Liu, S.; Fan, C.; et al. Emerging Organic Electrodes for Na-Ion and K-Ion Batteries. *Energy Storage Mater.* **2023**, *56*, 267–299. [CrossRef]
13. Wang, J.; Xu, Z.; Eloi, J.-C.; Titirici, M.-M.; Eichhorn, S.J. Ice-Templated, Sustainable Carbon Aerogels with Hierarchically Tailored Channels for Sodium- and Potassium-Ion Batteries. *Adv. Funct. Mater.* **2022**, *32*, 2110862. [CrossRef]
14. Mohan, I.; Raj, A.; Shubham, K.; Lata, D.B.; Mandal, S.; Kumar, S. Potential of Potassium and Sodium-Ion Batteries as the Future of Energy Storage: Recent Progress in Anodic Materials. *J. Energy Storage* **2022**, *55*, 105625. [CrossRef]
15. Bodart, J.; Eshraghi, N.; Sougrati, M.T.; Boschini, F.; Lippens, P.-E.; Vertruyen, B.; Mahmoud, A. From Na_2FePO_4F/CNT to $NaKFePO_4F/CNT$ as Advanced Cathode Material for K-Ion Batteries. *J. Power Sources* **2023**, *555*, 232410. [CrossRef]
16. Yao, K.; Wu, M.; Chen, D.; Liu, C.; Xu, C.; Yang, D.; Yao, H.; Liu, L.; Zheng, Y.; Rui, X. Vanadium Tetrasulfide for Next-Generation Rechargeable Batteries: Advances and Challenges. *Chem. Rec.* **2022**, *22*, 202200117. [CrossRef] [PubMed]
17. Yang, W.; Liu, Q.; Zhao, Y.; Mu, D.; Tan, G.; Gao, H.; Li, L.; Chen, R.; Wu, F. Progress on Fe-Based Polyanionic Oxide Cathodes Materials toward Grid-Scale Energy Storage for Sodium-Ion Batteries. *Small Methods* **2022**, *6*, 2200555. [CrossRef] [PubMed]
18. Zhang, Y.; Xu, J.; Li, Z.; Wang, Y.; Wang, S.; Dong, X.; Wang, Y. All-Climate Aqueous Na-Ion Batteries Using "Water-in-Salt" Electrolyte. *Sci. Bull.* **2022**, *67*, 161–170. [CrossRef]
19. Zhang, X.-L.; Huang, Z.-X.; Liu, Y.-N.; Su, M.-Y.; Li, K.; Wu, X.-L. Tuning Oxygen Release of Sodium-Ion Layered Oxide Cathode through Synergistic Surface Coating and Doping. *J. Colloid Interface Sci.* **2023**, *650*, 742–751. [CrossRef]
20. Guo, J.-Z.; Zhang, H.-X.; Gu, Z.-Y.; Du, M.; Lü, H.-Y.; Zhao, X.-X.; Yang, J.-L.; Li, W.-H.; Kang, S.; Zou, W.; et al. Heterogeneous NASICON-Type Composite as Low-Cost, High-Performance Cathode for Sodium-Ion Batteries. *Adv. Funct. Mater.* **2022**, *32*, 2209482. [CrossRef]
21. Chang, C.-B.; Tuan, H.-Y. Recent Progress on Sb- and Bi-Based Chalcogenide Anodes for Potassium-Ion Batteries. *Chem. Asian J.* **2022**, *17*, e202200170. [CrossRef]

22. Zhao, S.; Liu, Z.; Xie, G.; Guo, Z.; Wang, S.; Zhou, J.; Xie, X.; Sun, B.; Guo, S.; Wang, G. High-Efficiency Cathode Potassium Compensation and Interfacial Stability Improvement Enabled by Dipotassium Squarate for Potassium-Ion Batteries. *Energy Environ. Sci.* **2022**, *15*, 3015–3023. [CrossRef]

23. Gabriel, E.; Hou, D.; Lee, E.; Xiong, H. Multiphase Layered Transition Metal Oxide Positive Electrodes for Sodium Ion Batteries. *Energy Sci. Eng.* **2022**, *10*, 1672–1705. [CrossRef]

24. Liang, X.; Sun, Y.-K. A Novel Pentanary Metal Oxide Cathode with P2/O3 Biphasic Structure for High-Performance Sodium-Ion Batteries. *Adv. Funct. Mater.* **2022**, *32*, 2206154. [CrossRef]

25. Nathan, M.G.T.; Yu, H.; Kim, G.-T.; Kim, J.-H.; Cho, J.S.; Kim, J.; Kim, J.-K. Recent Advances in Layered Metal-Oxide Cathodes for Application in Potassium-Ion Batteries. *Adv. Sci.* **2022**, *9*, 2105882. [CrossRef] [PubMed]

26. Xiao, Z.; Xia, F.; Xu, L.; Wang, X.; Meng, J.; Wang, H.; Zhang, X.; Geng, L.; Wu, J.; Mai, L. Suppressing the Jahn–Teller Effect in Mn-Based Layered Oxide Cathode toward Long-Life Potassium-Ion Batteries. *Adv. Funct. Mater.* **2022**, *32*, 2108244. [CrossRef]

27. Zhang, K.-Y.; Gu, Z.-Y.; Ang, E.H.; Guo, J.-Z.; Wang, X.-T.; Wang, Y.; Wu, X.-L. Advanced Polyanionic Electrode Materials for Potassium-Ion Batteries: Progresses, Challenges and Application Prospects. *Mater. Today* **2022**, *54*, 189–201. [CrossRef]

28. Sun, X.; Li, Z.; Liu, Z.; Lv, X.; Shi, K.; Chen, R.; Wu, F.; Li, L. A New Candidate in Polyanionic Compounds for Potassium Ion Battery Anode: MXene Derived Carbon Coated π-Ti$_2$O(PO$_4$)$_2$. *Adv. Funct. Mater.* **2023**, *33*, 2300125. [CrossRef]

29. Xiao, L.; Ji, F.; Zhang, J.; Chen, X.; Fang, Y. Doping Regulation in Polyanionic Compounds for Advanced Sodium-Ion Batteries. *Small* **2023**, *19*, 2205732. [CrossRef]

30. Peng, J.; Zhang, W.; Liu, Q.; Wang, J.; Chou, S.; Liu, H.; Dou, S. Prussian Blue Analogues for Sodium-Ion Batteries: Past, Present, and Future. *Adv. Mater.* **2022**, *34*, 2108384. [CrossRef]

31. Li, Z.; Ozdogru, B.; Bal, B.; Bowden, M.; Choi, A.; Zhang, Y.; Wang, H.; Murugesan, V.; Pol, V.G.; Çapraz, Ö.Ö. The Role of Transition Metals on Chemo-Mechanical Instabilities in Prussian Blue Analogues For K-Ion Batteries: The Case Study on KNHCF Versus KMHCF. *Adv. Energy Mater.* **2023**, *13*, 2301329. [CrossRef]

32. Ge, J.; Fan, L.; Rao, A.M.; Zhou, J.; Lu, B. Surface-Substituted Prussian Blue Analogue Cathode for Sustainable Potassium-Ion Batteries. *Nat Sustain* **2022**, *5*, 225–234. [CrossRef]

33. Wang, J.; Liu, X.; Jia, H.; Apostol, P.; Guo, X.; Lucaccioni, F.; Zhang, X.; Zhu, Q.; Morari, C.; Gohy, J.-F.; et al. A High-Voltage Organic Framework for High-Performance Na- and K-Ion Batteries. *ACS Energy Lett.* **2022**, *7*, 668–674. [CrossRef]

34. Luo, X.-X.; Li, W.-H.; Liang, H.-J.; Zhang, H.-X.; Du, K.-D.; Wang, X.-T.; Liu, X.-F.; Zhang, J.-P.; Wu, X.-L. Covalent Organic Framework with Highly Accessible Carbonyls and π-Cation Effect for Advanced Potassium-Ion Batteries. *Angew. Chem.* **2022**, *134*, e202117661. [CrossRef]

35. Zhang, H.; Gao, Y.; Liu, X.-H.; Yang, Z.; He, X.-X.; Li, L.; Qiao, Y.; Chen, W.-H.; Zeng, R.-H.; Wang, Y.; et al. Organic Cathode Materials for Sodium-Ion Batteries: From Fundamental Research to Potential Commercial Application. *Adv. Funct. Mater.* **2022**, *32*, 2107718. [CrossRef]

36. Yabuuchi, N.; Kubota, K.; Dahbi, M.; Komaba, S. Research Development on Sodium-Ion Batteries. *Chem. Rev.* **2014**, *114*, 11636–11682. [CrossRef] [PubMed]

37. Rajagopalan, R.; Tang, Y.; Ji, X.; Jia, C.; Wang, H. Advancements and Challenges in Potassium Ion Batteries: A Comprehensive Review. *Adv. Funct. Mater.* **2020**, *30*, 1909486. [CrossRef]

38. Min, X.; Xiao, J.; Fang, M.; Wang, W.; Zhao, Y.; Liu, Y.; Abdelkader, A.M.; Xi, K.; Kumar, R.V.; Huang, Z. Potassium-Ion Batteries: Outlook on Present and Future Technologies. *Energy Environ. Sci.* **2021**, *14*, 2186–2243. [CrossRef]

39. Wu, Y.; Huang, H.-B.; Feng, Y.; Wu, Z.-S.; Yu, Y. The Promise and Challenge of Phosphorus-Based Composites as Anode Materials for Potassium-Ion Batteries. *Adv. Mater.* **2019**, *31*, 1901414. [CrossRef]

40. Lei, K.-X.; Wang, J.; Chen, C.; Li, S.-Y.; Wang, S.-W.; Zheng, S.-J.; Li, F.-J. Recent Progresses on Alloy-Based Anodes for Potassium-Ion Batteries. *Rare Met.* **2020**, *39*, 989–1004. [CrossRef]

41. Song, K.; Liu, C.; Mi, L.; Chou, S.; Chen, W.; Shen, C. Recent Progress on the Alloy-Based Anode for Sodium-Ion Batteries and Potassium-Ion Batteries. *Small* **2021**, *17*, 1903194. [CrossRef] [PubMed]

42. Liu, Y.; Liu, Q.; Zhang, A.; Cai, J.; Cao, X.; Li, Z.; Asimow, P.D.; Zhou, C. Room-Temperature Pressure Synthesis of Layered Black Phosphorus-Graphene Composite for Sodium-Ion Battery Anodes. *ACS Nano* **2018**, *12*, 8323–8329. [CrossRef] [PubMed]

43. Ni, J.; Li, X.; Sun, M.; Yuan, Y.; Liu, T.; Li, L.; Lu, J. Durian-Inspired Design of Bismuth–Antimony Alloy Arrays for Robust Sodium Storage. *ACS Nano* **2020**, *14*, 9117–9124. [CrossRef] [PubMed]

44. Zhu, J.; Liu, Z.; Wang, W.; Yue, L.; Li, W.; Zhang, H.; Zhao, L.; Zheng, H.; Wang, J.; Li, Y. Green, Template-Less Synthesis of Honeycomb-like Porous Micron-Sized Red Phosphorus for High-Performance Lithium Storage. *ACS Nano* **2021**, *15*, 1880–1892. [CrossRef] [PubMed]

45. Xiong, P.; Bai, P.; Li, A.; Li, B.; Cheng, M.; Chen, Y.; Huang, S.; Jiang, Q.; Bu, X.H.; Xu, Y. Bismuth Nanoparticle@Carbon Composite Anodes for Ultralong Cycle Life and High-Rate Sodium-Ion Batteries. *Adv. Mater.* **2019**, *31*, 1904771. [CrossRef] [PubMed]

46. Cheng, X.; Shao, R.; Li, D.; Yang, H.; Wu, Y.; Wang, B.; Sun, C.; Jiang, Y.; Zhang, Q.; Yu, Y. A Self-Healing Volume Variation Three-Dimensional Continuous Bulk Porous Bismuth for Ultrafast Sodium Storage. *Adv. Funct. Mater.* **2021**, *31*, 2011264. [CrossRef]

47. Cheng, X.; Sun, Y.; Li, D.; Yang, H.; Chen, F.; Huang, F.; Jiang, Y.; Wu, Y.; An, X.; Yu, Y. From 0D to 3D: Dimensional Control of Bismuth for Potassium Storage with Superb Kinetics and Cycling Stability. *Adv. Energy Mater.* **2021**, *11*, 2102263. [CrossRef]

48. Tian, X.; Zhang, P.; Liao, Y.; Soomro, R.A.; Xu, B. Achieving Stable and Ultrafast Potassium Storage of Antimony Anode via Dual Confinement of MXene@Carbon Framework. *Small Methods* **2023**, *7*, 2201525. [CrossRef]

49.   Zhang, X.; Qiu, X.; Lin, J.; Lin, Z.; Sun, S.; Yin, J.; Alshareef, H.N.; Zhang, W. Structure and Interface Engineering of Ultrahigh-Rate 3D Bismuth Anodes for Sodium-Ion Batteries. *Small* **2023**, *19*, 2302071. [CrossRef]

50.   Zhu, L.; Xu, K.; Fang, Y.; Wu, X.; Song, L.; Zhu, Y.; Qian, Y. Se-Induced Fibrous Nano Red P with Superior Conductivity for Sodium Batteries. *Adv. Funct. Mater.* **2023**, *33*, 2302444. [CrossRef]

51.   Xiao, W.; Li, X.; Cao, B.; Huang, G.; Xie, C.; Qin, J.; Yang, H.; Wang, J.; Sun, X. Constructing High-Rate and Long-Life Phosphorus/Carbon Anodes for Potassium-Ion Batteries through Rational Nanoconfinement. *Nano Energy* **2021**, *83*, 105772. [CrossRef]

52.   Hu, K.; Chen, Y.; Zheng, C.; Du, X.; Wang, M.; Yao, Q.; Wang, H.; Fan, K.; Wang, W.; Yan, X.; et al. Molten Salt-Assisted Synthesis of Bismuth Nanosheets with Long-Term Cyclability at High Rates for Sodium-Ion Batteries. *RSC Adv.* **2023**, *13*, 25552–25560. [CrossRef] [PubMed]

53.   Cheng, X.; Yang, H.; Wei, C.; Huang, F.; Yao, Y.; Bai, R.; Jiang, Y.; Li, S. Synergistic Effect of 1D Bismuth Nanowires/2D Graphene Composites for High Performance Flexible Anodes in Sodium-Ion Batteries. *J. Mater. Chem. A* **2023**, *11*, 8081–8090. [CrossRef]

54.   Pokropivny, V.V.; Skorokhod, V.V. Classification of Nanostructures by Dimensionality and Concept of Surface Forms Engineering in Nanomaterial Science. *Mater. Sci. Eng. C* **2007**, *27*, 990–993. [CrossRef]

55.   Xiong, P.; Bai, P.; Tu, S.; Cheng, M.; Zhang, J.; Sun, J.; Xu, Y. Red Phosphorus Nanoparticle@3D Interconnected Carbon Nanosheet Framework Composite for Potassium-Ion Battery Anodes. *Small* **2018**, *14*, 1802140. [CrossRef]

56.   Tian, W.; Zhang, S.; Huo, C.; Zhu, D.; Li, Q.; Wang, L.; Ren, X.; Xie, L.; Guo, S.; Chu, P.K.; et al. Few-Layer Antimonene: Anisotropic Expansion and Reversible Crystalline-Phase Evolution Enable Large-Capacity and Long-Life Na-Ion Batteries. *ACS Nano* **2018**, *12*, 1887–1893. [CrossRef]

57.   Shen, C.; Cheng, T.L.; Liu, C.Y.; Huang, L.; Cao, M.Y.; Song, G.Q.; Wang, D.; Lu, B.A.; Wang, J.W.; Qin, C.C.; et al. Bismuthene from Sonoelectrochemistry as a Superior Anode for Potassium-Ion Batteries. *J. Mater. Chem. A* **2020**, *8*, 453–460. [CrossRef]

58.   Liu, X.H.; Zhong, L.; Huang, S.; Mao, S.X.; Zhu, T.; Huang, J.Y. Size-Dependent Fracture of Silicon Nanoparticles during Lithiation. *ACS Nano* **2012**, *6*, 1522–1531. [CrossRef]

59.   Liu, W.; Ju, S.; Yu, X. Phosphorus-Amine-Based Synthesis of Nanoscale Red Phosphorus for Application to Sodium-Ion Batteries. *ACS Nano* **2020**, *14*, 974–984. [CrossRef]

60.   Zhu, Z.; Pei, Z.; Liu, B.; Sun, D.; Fang, Y.; Lei, X.; Liu, X.; Niu, S.; Pan, H.; Zhou, J.; et al. Hierarchical Ion/Electron Networks Enable Efficient Red Phosphorus Anode with High Mass Loading for Sodium Ion Batteries. *Adv. Funct. Mater.* **2022**, *32*, 2110444. [CrossRef]

61.   Ma, X.; Ji, C.; Li, X.; Liu, Y.; Xiong, X. Red@Black Phosphorus Core–Shell Heterostructure with Superior Air Stability for High-Rate and Durable Sodium-Ion Battery. *Mater. Today* **2022**, *59*, 36–45. [CrossRef]

62.   Liu, D.; Huang, X.; Qu, D.; Zheng, D.; Wang, G.; Harris, J.; Si, J.; Ding, T.; Chen, J.; Qu, D. Confined Phosphorus in Carbon Nanotube-Backboned Mesoporous Carbon as Superior Anode Material for Sodium/Potassium-Ion Batteries. *Nano Energy* **2018**, *52*, 1–10. [CrossRef]

63.   Zhu, H.; Wang, F.; Peng, L.; Qin, T.; Kang, F.; Yang, C. Inlaying Bismuth Nanoparticles on Graphene Nanosheets by Chemical Bond for Ultralong-Lifespan Aqueous Sodium Storage. *Angew. Chem., Int. Ed.* **2023**, *62*, e202212439. [CrossRef] [PubMed]

64.   Zhao, Y.; Ren, X.; Xing, Z.; Zhu, D.; Tian, W.; Guan, C.; Yang, Y.; Qin, W.; Wang, J.; Zhang, L.; et al. In Situ Formation of Hierarchical Bismuth Nanodots/Graphene Nanoarchitectures for Ultrahigh-Rate and Durable Potassium-Ion Storage. *Small* **2020**, *16*, 1905789. [CrossRef] [PubMed]

65.   Xiong, P.; Wu, J.; Zhou, M.; Xu, Y. Bismuth-Antimony Alloy Nanoparticle@Porous Carbon Nanosheet Composite Anode for High-Performance Potassium-Ion Batteries. *ACS Nano* **2020**, *14*, 1018–1026. [CrossRef] [PubMed]

66.   Yang, X.; Zhang, R. High-Capacity Graphene-Confined Antimony Nanoparticles as a Promising Anode Material for Potassium-Ion Batteries. *J. Alloys Compd.* **2020**, *834*, 155191. [CrossRef]

67.   Yang, Y.; Zhang, W.; Liu, Y.; Li, L.; Zhao, X.; Zhang, W. Antimony/Polypyrrole/CNTs Composites with Three-Dimensional Structure as Highly Stable Anodes for Potassium Ion Battery. *Mater. Res. Bull.* **2023**, *168*, 112496. [CrossRef]

68.   Yu, J.; Zhao, D.; Ma, C.; Feng, L.; Zhang, Y.; Zhang, L.; Liu, Y.; Guo, S. Vapor-Phase Derived Ultra-Fine Bismuth Nanoparticles Embedded in Carbon Nanotube Networks as Anodes for Sodium and Potassium Ion Batteries. *J. Colloid Interface Sci.* **2023**, *643*, 409–419. [CrossRef]

69.   Yao, T.; Li, L.; Wang, H. Embedding Antimony Nanoparticles into Metal-Organic Framework Derived TiO_2@carbon Nanotablets for High-Performance Sodium Storage. *Chin. Chem. Lett.* **2023**, *34*, 108186. [CrossRef]

70.   Arnold, S.; Gentile, A.; Li, Y.; Wang, Q.; Marchionna, S.; Ruffo, R.; Presser, V. Design of High-Performance Antimony/MXene Hybrid Electrodes for Sodium-Ion Batteries. *J. Mater. Chem. A* **2022**, *10*, 10569–10585. [CrossRef]

71.   Guo, X.; Gao, H.; Wang, S.; Yang, G.; Zhang, X.; Zhang, J.; Liu, H.; Wang, G. MXene-Based Aerogel Anchored with Antimony Single Atoms and Quantum Dots for High-Performance Potassium-Ion Batteries. *Nano Lett.* **2022**, *22*, 1225–1232. [CrossRef] [PubMed]

72.   Zheng, J.; Yang, Y.; Fan, X.; Ji, G.; Ji, X.; Wang, H.; Hou, S.; Zachariah, M.R.; Wang, C. Extremely Stable Antimony–Carbon Composite Anodes for Potassium-Ion Batteries. *Energy Environ. Sci.* **2019**, *12*, 615–623. [CrossRef]

73.   Chen, B.; Zhang, H.; Liang, M.; Wang, Y.; Wu, Z.; Zhu, S.; Shi, C.; Zhao, N.; Liu, E.; Sow, C.H.; et al. NaCl-Pinned Antimony Nanoparticles Combined with Ion-Shuttle-Induced Graphitized 3D Carbon to Boost Sodium Storage. *Cell Rep. Phys. Sci.* **2022**, *3*, 100891. [CrossRef]

74. Huang, H.; Wang, J.; Yang, X.; Hu, R.; Liu, J.; Zhang, L.; Zhu, M. Unveiling the Advances of Nanostructure Design for Alloy-Type Potassium-Ion Battery Anodes via In Situ TEM. *Angew. Chem.* **2020**, *132*, 14612–14618. [CrossRef]

75. Li, W.-J.; Chou, S.-L.; Wang, J.-Z.; Liu, H.-K.; Dou, S.-X. Simply Mixed Commercial Red Phosphorus and Carbon Nanotube Composite with Exceptionally Reversible Sodium-Ion Storage. *Nano Lett.* **2013**, *13*, 5480–5484. [CrossRef] [PubMed]

76. Song, J.; Yu, Z.; Gordin, M.L.; Li, X.; Peng, H.; Wang, D. Advanced Sodium Ion Battery Anode Constructed via Chemical Bonding between Phosphorus, Carbon Nanotube, and Cross-Linked Polymer Binder. *ACS Nano* **2015**, *9*, 11933–11941. [CrossRef] [PubMed]

77. Xu, G.-L.; Chen, Z.; Zhong, G.-M.; Liu, Y.; Yang, Y.; Ma, T.; Ren, Y.; Zuo, X.; Wu, X.-H.; Zhang, X.; et al. Nanostructured Black Phosphorus/Ketjenblack–Multiwalled Carbon Nanotubes Composite as High Performance Anode Material for Sodium-Ion Batteries. *Nano Lett.* **2016**, *16*, 3955–3965. [CrossRef]

78. Liu, W.; Yuan, X.; Yu, X. A Core–Shell Structure of Polydopamine-Coated Phosphorus–Carbon Nanotube Composite for High-Performance Sodium-Ion Batteries. *Nanoscale* **2018**, *10*, 16675–16682. [CrossRef]

79. Li, J.; Jin, H.; Yuan, Y.; Lu, H.; Su, C.; Fan, D.; Li, Y.; Wang, J.; Lu, J.; Wang, S. Encapsulating Phosphorus inside Carbon Nanotubes via a Solution Approach for Advanced Lithium Ion Host. *Nano Energy* **2019**, *58*, 23–29. [CrossRef]

80. Liu, Y.; Liu, Q.; Jian, C.; Cui, D.; Chen, M.; Li, Z.; Li, T.; Nilges, T.; He, K.; Jia, Z.; et al. Red-Phosphorus-Impregnated Carbon Nanofibers for Sodium-Ion Batteries and Liquefaction of Red Phosphorus. *Nat. Commun.* **2020**, *11*, 2520. [CrossRef]

81. Xiang, X.; Liu, D.; Zhu, X.; Fang, K.; Zhou, K.; Tang, H.; Xie, Z.; Li, J.; Zheng, H.; Qu, D. Evaporation-Induced Formation of Hollow bismuth@N-Doped Carbon Nanorods for Enhanced Electrochemical Potassium Storage. *Appl. Surf. Sci.* **2020**, *514*, 145947. [CrossRef]

82. Imtiaz, S.; Kapuria, N.; Amiinu, I.S.; Sankaran, A.; Singh, S.; Geaney, H.; Kennedy, T.; Ryan, K.M. Directly Deposited Antimony on Copper Silicide Nanowire Array as High-Performance Potassium-Ion Battery Anode with Long Cycle Life. *Adv. Funct. Mater.* **2023**, *33*, 2209566. [CrossRef]

83. Pu, B.; Liu, Y.; Bai, J.; Chu, X.; Zhou, X.; Qing, Y.; Wang, Y.; Zhang, M.; Ma, Q.; Xu, Z.; et al. Iodine-Ion-Assisted Galvanic Replacement Synthesis of Bismuth Nanotubes for Ultrafast and Ultrastable Sodium Storage. *ACS Nano* **2022**, *16*, 18746–18756. [CrossRef] [PubMed]

84. Li, X.; Xiao, S.; Niu, X.; Chen, J.S.; Yu, Y. Efficient Stress Dissipation in Well-Aligned Pyramidal SbSn Alloy Nanoarrays for Robust Sodium Storage. *Adv. Funct. Mater.* **2021**, *31*, 2104798. [CrossRef]

85. Song, T.; Chen, H.; Li, Z.; Xu, Q.; Liu, H.; Wang, Y.; Xia, Y. Creating an Air-Stable Sulfur-Doped Black Phosphorus-TiO2 Composite as High-Performance Anode Material for Sodium-Ion Storage. *Adv. Funct. Mater.* **2019**, *29*, 1900535. [CrossRef]

86. Wu, S.; Hui, K.S.; Hui, K.N. 2D Black Phosphorus: From Preparation to Applications for Electrochemical Energy Storage. *Adv. Sci.* **2018**, *5*, 1700491. [CrossRef] [PubMed]

87. Liu, H.; Neal, A.T.; Zhu, Z.; Luo, Z.; Xu, X.; Tománek, D.; Ye, P.D. Phosphorene: An Unexplored 2D Semiconductor with a High Hole Mobility. *ACS Nano* **2014**, *8*, 4033–4041. [CrossRef]

88. Xia, F.; Wang, H.; Jia, Y. Rediscovering Black Phosphorus as an Anisotropic Layered Material for Optoelectronics and Electronics. *Nat. Commun.* **2014**, *5*, 4458. [CrossRef]

89. Sun, J.; Lee, H.-W.; Pasta, M.; Yuan, H.; Zheng, G.; Sun, Y.; Li, Y.; Cui, Y. A Phosphorene–Graphene Hybrid Material as a High-Capacity Anode for Sodium-Ion Batteries. *Nat. Nanotech.* **2015**, *10*, 980–985. [CrossRef]

90. Shuai, H.; Ge, P.; Hong, W.; Li, S.; Hu, J.; Hou, H.; Zou, G.; Ji, X. Electrochemically Exfoliated Phosphorene–Graphene Hybrid for Sodium-Ion Batteries. *Small Methods* **2019**, *3*, 1800328. [CrossRef]

91. Guo, X.; Zhang, W.; Zhang, J.; Zhou, D.; Tang, X.; Xu, X.; Li, B.; Liu, H.; Wang, G. Boosting Sodium Storage in Two-Dimensional Phosphorene/Ti3C2Tx MXene Nanoarchitectures with Stable Fluorinated Interphase. *ACS Nano* **2020**, *14*, 3651–3659. [CrossRef] [PubMed]

92. Zhang, J.L.; Zhao, S.; Han, C.; Wang, Z.; Zhong, S.; Sun, S.; Guo, R.; Zhou, X.; Gu, C.D.; Yuan, K.D.; et al. Epitaxial Growth of Single Layer Blue Phosphorus: A New Phase of Two-Dimensional Phosphorus. *Nano Lett.* **2016**, *16*, 4903–4908. [CrossRef]

93. Fan, K.; Tang, T.; Wu, S.; Zhang, Z. Graphene/Blue-Phosphorus Heterostructure as Potential Anode Materials for Sodium-Ion Batteries. *Int. J. Mod. Phys. B* **2018**, *32*, 1850010. [CrossRef]

94. Gibaja, C.; Rodriguez-San-Miguel, D.; Ares, P.; Gómez-Herrero, J.; Varela, M.; Gillen, R.; Maultzsch, J.; Hauke, F.; Hirsch, A.; Abellán, G.; et al. Few-Layer Antimonene by Liquid-Phase Exfoliation. *Angew. Chem.* **2016**, *128*, 14557–14561. [CrossRef]

95. Ares, P.; Aguilar-Galindo, F.; Rodríguez-San-Miguel, D.; Aldave, D.A.; Díaz-Tendero, S.; Alcamí, M.; Martín, F.; Gómez-Herrero, J.; Zamora, F. Mechanical Isolation of Highly Stable Antimonene under Ambient Conditions. *Adv. Mater.* **2016**, *28*, 6332–6336. [CrossRef] [PubMed]

96. Wu, X.; Shao, Y.; Liu, H.; Feng, Z.; Wang, Y.-L.; Sun, J.-T.; Liu, C.; Wang, J.-O.; Liu, Z.-L.; Zhu, S.-Y.; et al. Epitaxial Growth and Air-Stability of Monolayer Antimonene on PdTe2. *Adv. Mater.* **2017**, *29*, 1605407. [CrossRef] [PubMed]

97. Ji, J.; Song, X.; Liu, J.; Yan, Z.; Huo, C.; Zhang, S.; Su, M.; Liao, L.; Wang, W.; Ni, Z.; et al. Two-Dimensional Antimonene Single Crystals Grown by van Der Waals Epitaxy. *Nat. Commun.* **2016**, *7*, 13352. [CrossRef]

98. Liu, H.; Lian, P.; Zhang, Q.; Yang, Y.; Mei, Y. The Preparation of Holey Phosphorene by Electrochemical Assistance. *Electrochem. Commun.* **2019**, *98*, 124–128. [CrossRef]

99. Liu, X.; Zhang, S.; Guo, S.; Cai, B.; Yang, S.A.; Shan, F.; Pumera, M.; Zeng, H. Advances of 2D Bismuth in Energy Sciences. *Chem. Soc. Rev.* **2020**, *49*, 263–285. [CrossRef]

100. Zhang, R.; Yang, Y.; Guo, L.; Luo, Y. A Fast and High-Efficiency Electrochemical Exfoliation Strategy towards Antimonene/Carbon Composites for Selective Lubrication and Sodium–Ion Storage Applications. *Phys. Chem. Chem. Phys.* **2022**, *24*, 4957–4965. [CrossRef]

101. Girirajan, M.; Arumugam, V.; Subramaniyan, S.; Manimuthu, R.P.; Sakkarapani, S. Two-Dimensional Layered Bismuthene/Antimonene Nanocomposite as a Potential Electrode Material for the Fabrication of High-Energy Density Hybrid Supercapacitors. *Energy Fuels* **2022**, *36*, 12299–12309. [CrossRef]

102. Yang, J.; Wang, X.; Qu, Y.; Wang, X.; Huo, H.; Fan, Q.; Wang, J.; Yang, L.-M.; Wu, Y. Bi-Based Metal-Organic Framework Derived Leafy Bismuth Nanosheets for Carbon Dioxide Electroreduction. *Adv. Energy Mater.* **2020**, *10*, 2001709. [CrossRef]

103. Wei, S.; Li, W.; Ma, Z.; Deng, X.; Li, Y.; Wang, X. Novel Bismuth Nanoflowers Encapsulated in N-Doped Carbon Frameworks as Superb Composite Anodes for High-Performance Sodium-Ion Batteries. *Small* **2023**, *19*, 2304265. [CrossRef]

104. Liu, X.; Xiao, B.; Daali, A.; Zhou, X.; Yu, Z.; Li, X.; Liu, Y.; Yin, L.; Yang, Z.; Zhao, C.; et al. Stress- and Interface-Compatible Red Phosphorus Anode for High-Energy and Durable Sodium-Ion Batteries. *ACS Energy Lett.* **2021**, *6*, 547–556. [CrossRef]

105. Liu, W.; Du, L.; Ju, S.; Cheng, X.; Wu, Q.; Hu, Z.; Yu, X. Encapsulation of Red Phosphorus in Carbon Nanocages with Ultrahigh Content for High-Capacity and Long Cycle Life Sodium-Ion Batteries. *ACS Nano* **2021**, *15*, 5679–5688. [CrossRef] [PubMed]

106. Wang, C.; Wang, L.; Li, F.; Cheng, F.; Chen, J. Bulk Bismuth as a High-Capacity and Ultralong Cycle-Life Anode for Sodium-Ion Batteries by Coupling with Glyme-Based Electrolytes. *Adv. Mater.* **2017**, *29*, 1702212. [CrossRef] [PubMed]

107. Guo, S.; Wei, C.; Wang, L.; Mei, S.; Xiang, B.; Zheng, Y.; Zhang, X.; Javanbakht, M.; Gao, B.; Chu, P.K.; et al. Micro-Sized Porous Bulk Bismuth Caged by Carbon for Fast Charging and Ultralong Cycling in Sodium-Ion Batteries. *Cell Rep. Phys. Sci.* **2023**, *4*, 101463. [CrossRef]

108. An, Y.; Tian, Y.; Ci, L.; Xiong, S.; Feng, J.; Qian, Y. Micron-Sized Nanoporous Antimony with Tunable Porosity for High-Performance Potassium-Ion Batteries. *ACS Nano* **2018**, *12*, 12932–12940. [CrossRef]

109. Gao, H.; Niu, J.; Zhang, C.; Peng, Z.; Zhang, Z. A Dealloying Synthetic Strategy for Nanoporous Bismuth-Antimony Anodes for Sodium Ion Batteries. *ACS Nano* **2018**, *12*, 3568–3577. [CrossRef]

110. Wang, L.; Ni, Y.; Lei, K.; Dong, H.; Tian, S.; Li, F. 3D Porous Tin Created by Tuning the Redox Potential Acts as an Advanced Electrode for Sodium-Ion Batteries. *ChemSusChem* **2018**, *11*, 3376–3381. [CrossRef]

111. Liu, B.; Zhang, Q.; Li, L.; Jin, Z.; Wang, C.; Zhang, L.; Su, Z.-M. Encapsulating Red Phosphorus in Ultralarge Pore Volume Hierarchical Porous Carbon Nanospheres for Lithium/Sodium-Ion Half/Full Batteries. *ACS Nano* **2019**, *13*, 13513–13523. [CrossRef]

112. Wu, Y.; Xing, F.; Xu, R.; Cheng, X.; Li, D.; Zhou, X.; Zhang, Q.; Yu, Y. Spatially Confining and Chemically Bonding Amorphous Red Phosphorus in the Nitrogen Doped Porous Carbon Tubes Leading to Superior Sodium Storage Performance. *J. Mater. Chem. A* **2019**, *7*, 8581–8588. [CrossRef]

113. Li, W.; Han, C.; Gu, Q.; Chou, S.; Liu, H.K.; Dou, S.X. Three-Dimensional Electronic Network Assisted by TiN Conductive Pillars and Chemical Adsorption to Boost the Electrochemical Performance of Red Phosphorus. *ACS Nano* **2020**, *14*, 4609–4617. [CrossRef] [PubMed]

114. Liu, S.; Xu, H.; Bian, X.; Feng, J.; Liu, J.; Yang, Y.; Yuan, C.; An, Y.; Fan, R.; Ci, L. Nanoporous Red Phosphorus on Reduced Graphene Oxide as Superior Anode for Sodium-Ion Batteries. *ACS Nano* **2018**, *12*, 7380–7387. [CrossRef] [PubMed]

115. Liu, X.; Zhu, J.; Wang, X.; Yue, L.; Wang, W.; Wang, B.; Shen, D.; Li, Y. Boosting Potassium Storage Kinetics, Stability, and Volumetric Performance of Honeycomb-Like Porous Red Phosphorus via In Situ Embedding Self-Growing Conductive Nano-Metal Networks. *Adv. Funct. Mater.* **2023**, *33*, 2209388. [CrossRef]

116. Liu, Y.; Zhang, N.; Jiao, L.; Tao, Z.; Chen, J. Ultrasmall Sn Nanoparticles Embedded in Carbon as High-Performance Anode for Sodium-Ion Batteries. *Adv. Funct. Mater.* **2015**, *25*, 214–220. [CrossRef]

117. Chen, S.; Ao, Z.; Sun, B.; Xie, X.; Wang, G. Porous Carbon Nanocages Encapsulated with Tin Nanoparticles for High Performance Sodium-Ion Batteries. *Energy Storage Mater.* **2016**, *5*, 180–190. [CrossRef]

118. He, W.; Chen, K.; Pathak, R.; Hummel, M.; Reza, K.M.; Ghimire, N.; Pokharel, J.; Lu, S.; Gu, Z.; Qiao, Q.; et al. High-Mass-Loading Sn-Based Anode Boosted by Pseudocapacitance for Long-Life Sodium-Ion Batteries. *Chem. Eng. J.* **2021**, *414*, 128638. [CrossRef]

119. Yang, J.; Guo, X.; Gao, H.; Wang, T.; Liu, Z.; Yang, Q.; Yao, H.; Li, J.; Wang, C.; Wang, G. A High-Performance Alloy-Based Anode Enabled by Surface and Interface Engineering for Wide-Temperature Sodium-Ion Batteries. *Adv. Energy Mater.* **2023**, *13*, 2300351. [CrossRef]

120. Nam, D.-H.; Kim, T.-H.; Hong, K.-S.; Kwon, H.-S. Template-Free Electrochemical Synthesis of Sn Nanofibers as High-Performance Anode Materials for Na-Ion Batteries. *ACS Nano* **2014**, *8*, 11824–11835. [CrossRef]

121. Zhu, Y.; Yao, Q.; Shao, R.; Wang, C.; Yan, W.; Ma, J.; Liu, D.; Yang, J.; Qian, Y. Microsized Gray Tin as a High-Rate and Long-Life Anode Material for Advanced Sodium-Ion Batteries. *Nano Lett.* **2022**, *22*, 7976–7983. [CrossRef] [PubMed]

122. Zhou, L.; Cao, Z.; Zhang, J.; Cheng, H.; Liu, G.; Park, G.-T.; Cavallo, L.; Wang, L.; Alshareef, H.N.; Sun, Y.-K.; et al. Electrolyte-Mediated Stabilization of High-Capacity Micro-Sized Antimony Anodes for Potassium-Ion Batteries. *Adv. Mater.* **2021**, *33*, 2005993. [CrossRef] [PubMed]

123. Yang, H.; Xu, R.; Yao, Y.; Ye, S.; Zhou, X.; Yu, Y. Multicore–Shell Bi@N-Doped Carbon Nanospheres for High Power Density and Long Cycle Life Sodium- and Potassium-Ion Anodes. *Adv. Funct. Mater.* **2019**, *29*, 1809195. [CrossRef]

124. Huang, J.; Lin, X.; Tan, H.; Zhang, B. Bismuth Microparticles as Advanced Anodes for Potassium-Ion Battery. *Adv. Energy Mater.* **2018**, *8*, 1703496. [CrossRef]